

Original

Zhang, W.; Cui, Y.; Santos, A.I.; Hanebuth, T.J.J.:
Storm-driven bottom sediment transport on a high-energy narrow shelf (NW Iberia) and development of mud depocenters
Journal of Geophysical Research : Oceans (2016) AGU

DOI: 10.1002/2015JC011526

RESEARCH ARTICLE

10.1002/2015JC011526

Storm-driven bottom sediment transport on a high-energy narrow shelf (NW Iberia) and development of mud depocenters

Wenyan Zhang^{1,2}, Yongsheng Cui³, Ana I. Santos⁴, and Till J. J. Hanebuth^{1,5}

Key Points:

- Storm-driven bottom sediment transport on a narrow shelf was monitored and modelled
- Downwelling front and coastal jet greatly shape mid-shelf mud depocenters
- Shoreward boundary of mud depocenters coincides seaward limit of downwelling fronts
- Resolving near-bottom SPM transport is key to understanding mud depocenters

Supporting Information:

- Supporting Information S1

Correspondence to:

W. Zhang,
wenyan.zhang@hzg.de

Citation:

Zhang, W., Y. Cui, A. I. Santos, and T. J. J. Hanebuth (2016), Storm-driven bottom sediment transport on a high-energy narrow shelf (NW Iberia) and development of mud depocenters, *J. Geophys. Res. Oceans*, 121, 5751–5772, doi:10.1002/2015JC011526.

Received 4 DEC 2015

Accepted 15 JUL 2016

Accepted article online 20 JUL 2016

Published online 11 AUG 2016

¹MARUM—Center for Marine Environmental Sciences, University of Bremen, Bremen, Germany, ²Institute of Coastal Research, Helmholtz-Zentrum Geesthacht, Geesthacht, Germany, ³Center for Coastal Ocean Science and Technology, Sun Yat-sen University, Guangzhou, China, ⁴Marinha—Instituto Hidrográfico, Lisbon, Portugal, ⁵School of Coastal and Marine Systems Science, Coastal Carolina University, Conway, South Carolina, USA

Abstract Bottom sediment transport on the NW Iberian shelf was monitored during a downwelling storm in September 2014. Collected data were analyzed and fed into a 3-D coastal ocean model to understand storm-driven sediment transport on the shelf and its impact on midshelf mud depocenters (MDCs). A significantly enhanced level of bottom sediment resuspension, nearly two orders of magnitude higher than that in the prestorm period, was recorded at the mooring site. Field data analysis reveals that it was induced by a short-lasting strong bottom current in combination with enhanced wave-current interaction. Simulation results indicate that this strong current was part of a coastal jet resulted from downwelling. An across-shelf horizontal density gradient as high as 0.32 g/m^4 occurred at the interface between the downwelling and the bottom waters, forming a remarkable front. Due to buoyancy effect, the downwelling water was mostly confined to the coast with a depth limit of 80 m in the south and 120 m in the north of the region, resulting in a northward-directed coastal jet. Simulation results suggest that during the storm, local near-bottom sediment suspensions with concentrations on the order of 10 kg/m^3 would be triggered by wave-current interaction and flow convergence associated with the front. Direct impact on the development of MDCs by transport and deposition of concentrated sediment suspensions is indicated by model results. The seaward limit of the front coincided with the shoreward edge of the MDC nucleus, suggesting the front as a primary control on the deposition of fine-grained sediment.

1. Introduction

Three primary means, i.e., (a) surface buoyancy plume (hypopycnal) dispersal, (b) dilute suspension dispersal in the bottom-boundary layer, and (c) gravity-driven turbidity (hyperpycnal) flows have been suggested to be responsible for transporting fine-grained sediment (mud to fine sand) across continental shelves [Walsh and Nittrouer, 2009]. Whilst the first two means of sediment transport have been documented extensively [e.g., McCave, 1973; Colby, 1956; Wright, 1977; Cacchione et al., 1987; Fredsoe and Deigaard, 1992; Nielsen, 1992; van Rijn, 1993; Nittrouer and Wright, 1994; Bursik, 1995; Bennett et al., 1998; Syvitski and Morehead, 1999; Hill and McCave, 2001; Geyer et al., 2004; McKee et al., 2004; Moriarty et al., 2014], mechanisms for triggering and maintaining a gravity-driven turbidity flow on relatively flat (slope less than 0.012) continental shelves and its quantitative contribution to across-shelf sediment transport have recently started to attract considerable interest [e.g., Trowbridge and Kineke, 1994; Kineke et al., 1996, 2000; Sternberg et al., 1996, 2001; Ogston et al., 2000; Traykovski et al., 2000, 2007; Wright et al., 2001; Scully et al., 2003; Friedrichs and Wright, 2004; Dalrymple and Cummings, 2005; Harris et al., 2005; Hsu et al., 2009; Macquaker et al., 2010; Ozdemir et al., 2010; Corbett et al., 2014; Kampf and Myrow, 2014; Hale and Ogston, 2015; Hooshmand et al., 2015].

Although seen from aerial photos, surface buoyancy plume dispersal contributes to only a minor portion of across-shelf sediment transport [Geyer et al., 2004; Walsh and Nittrouer, 2009]. In most cases, it is found that the near-bottom dispersal, including both dilute suspension in the Bottom Boundary Layer (BBL) and concentrated turbidity flows confined to a very thin layer above seafloor (i.e., the wave boundary layer), is the dominant cause of across-shelf sediment transport, and the latter is especially responsible for emplacement of flood deposits on many muddy shelves [Wright and Friedrichs, 2006]. Deposits from wave and current-supported turbidity flows (WCSTFs hereafter) provide a sound explanation for the existence of stratification in fine-grained sediment successions found in very low-gradient shelf slope settings [e.g., Varban and Plint,

2008; *Ichaso and Dalrymple, 2009*], though it is not always straightforward to directly link these sediment intercalations in modern fine-grained deposits or ancient shales with this driving mechanism [*Macquaker et al., 2010*].

Near-bottom sediment dispersal and accumulation create morphological features that give shape to continental margin surfaces. Large-scale (10–100 km long) midshelf mud depocenters (MDCs) distributed worldwide [e.g., *Hanebuth et al., 2015c*] represent a typical example of such features. MDCs serve as cradles of life due to their comparably calm bottom conditions [e.g., *Rosenberg, 2001*], and represent a major sink for continental material supplied by rivers to the ocean [e.g., *Hanebuth et al., 2015c*]. MDCs often appear in the form of elongated belts and are highly vulnerable to environmental changes [*Gao and Collins, 2014*]. Thus the sedimentary history preserved in MDCs contains valuable information for material budgeting of the global source-to-sink system and environmental variability [e.g., *Naughton et al., 2007; Sommerfield and Wheatcroft, 2007; Hanebuth and Lantzsch, 2008; Oberle et al., 2014*]. Despite their remarkable potential as environmental archives and their critical role for the global source-to-sink system, the driving forces that control formation and evolution of MDCs are still poorly understood [*Walsh and Nittrouer, 2009; Gao and Collins, 2014*]. It has been suggested that the WCSTFs play an important role for the generation of mid-shelf mud depocenters [*Wright and Friedrichs, 2006*]. Their imprint in sedimentary MDC record is, however, commonly very subtle [*Macquaker et al., 2010*] and most existing studies interpreted them in an inappropriate spatial resolution (e.g., from seismic profiles) which is too coarse to discern individual layers. The difficulty to trace the impacts of WCSTFs on the development of MDCs is due to the fact that seafloor surface sediments are frequently reworked by physical as well as biological processes and might undergo many cycles of resuspension-transport-deposition before they get ultimately buried and incorporated into the long-term sedimentary record. Thus the thickness of the preserved layers that result directly from the WCSTFs is normally in the order of mm and the layers are often intercalated with sediment dispersed by other processes [*Macquaker et al., 2010*]. The effect of WCSTFs alone can, thus, not fully explain the formation and evolution of MDCs and other near-bottom processes (e.g., wave-current interaction, bottom Ekman transport, and secondary circulations) need to be taken into account in order to derive a comprehensive understanding of the morphodynamics of MDCs.

This paper aims to tackle the challenges in understanding storm-driven bottom sediment transport on the continental shelf and its direct influence on the development of MDCs. We present a case study of the NW Iberian shelf by combining the analysis of field data collected during a research cruise M110 GALIMOS (Monitoring the interaction between Oceanographic elements and Sedimentary seabed structures at the GALlician margin; 14–30 September 2014, with the German R/V METEOR; [*Hanebuth et al., 2015a*]) with simulation results from a three-dimensional coastal ocean model. The time span of investigation covers the entire phase of a storm passing through the study area (i.e., from arrival of the storm front to post-storm relaxation) and therefore the data are of high value for the assessment of storm impacts on bottom sediment transport around MDCs.

2. Study Area and Oceanographic Setting

The study area off the north-western Iberian Peninsula, namely Galicia and the northernmost part of Portugal, is a representative example of the eastern Atlantic continental margin that is characterized by a relatively narrow shelf (width less than 40 km) and a steep ($> 20^\circ$) continental slope (Figure 1a). The broad aspects of the shelf dynamics in this region are mainly attributed to the seasonal variation of two major atmospheric systems in the north Atlantic: the Azores High and the Iceland Low [*Wooster et al., 1976*]. As a result two mean circulation patterns, with summer upwelling from April to September and winter downwelling from October to March, develop with interannual variability in the intensity and timing. In summer, the hydrodynamic regime on the shelf is relatively calm, characterized by a mild equatorward-directed alongshore current and low-energy waves with significant wave heights typically below 3 m [*PO-WAVES Group, 1994*]. In winter, the hydrodynamic regime on the shelf becomes energetic, characterized by episodically strong poleward-directed wind-driven currents and increasing wave heights. This transition between the two seasons is due to a southward shift of low pressure systems (e.g., storms) that are mainly constrained to the north of the Iberian Peninsula in the summer season [*Wooster et al., 1976*]. Significant wave heights often exceed 5 m during storms, with an intense interaction between swells and storm-generated local waves

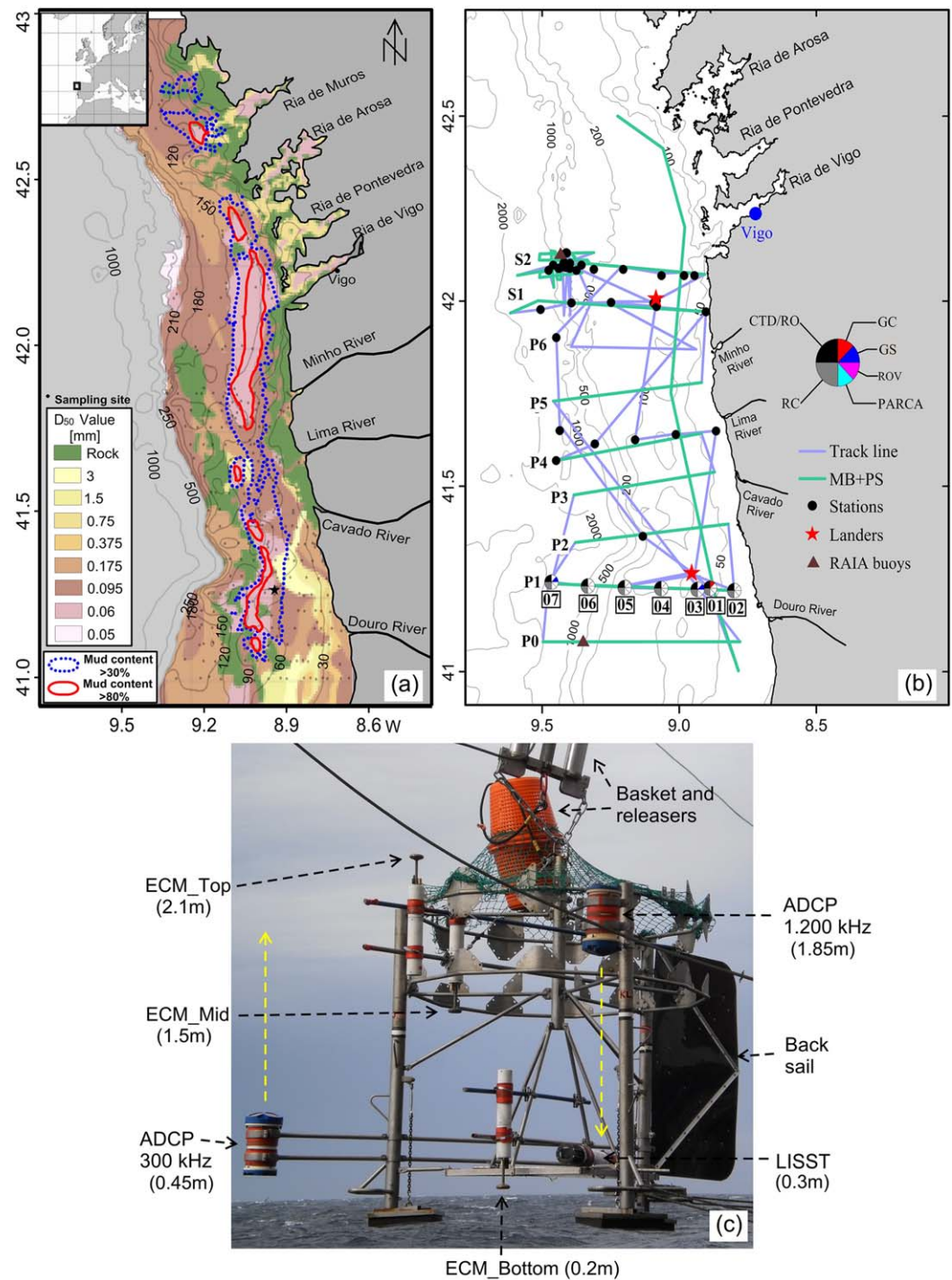


Figure 1. (a) Map of the study area showing the distribution of surface sediment median grain size. Mud depocenters are delineated by the dashed line (mud content $>30\%$) and the solid line (mud content $>80\%$). The map is modified from *Dias et al.* [2002b]. (b) Sketch map of the M110 GALIMOS cruise showing the track lines with SADC (75 kHz), multibeam (MB), and sediment echo-sounding (PS) data, location of stations (CTD/RO: CTD Rosette; GC: gravity corer; GS: grab sampler; ROV: remotely operating vehicle; PARCA: particle camera; RC: Rumohr Corer), lander deployments, and sea surface buoys (RAIA: Oceanic observatory for the Iberian shelf, <http://www.observatorioraia.org>). (c) Photograph of the lander and its instrumentation. Distance of each instrument from the bottom of the lander is also indicated.

that can lead to maximum wave heights over 10 m on the midshelf [PO-WAVES Group, 1994; Vitorino et al., 2002a]. Heavy precipitation often accompanies the low pressure systems, resulting in extreme values of river runoff during winter [Otero et al., 2010]. Among various riverine sources (i.e., four main rivers in the

southern part of the study area plus small rivers in the Galician Rias, as shown in Figure 1a) that supply fresh water and terrestrial sediment to the shelf, the Douro River contributes the most significant portion (~60%), with a daily mean discharge value of 710 m³/s and extreme value up to 19,000 m³/s during floods [Oliveira *et al.*, 2002]. The combination of enhanced river supply and highly energetic hydrodynamic conditions should both play an essential role in introducing and distributing sediment over the entire shelf, as is the case in many other shelves where WCSTFs are active and MDCs are found (e.g., see the compilation by Wright and Friedrichs [2006]). However, due to a massive construction of dams along the rivers (e.g., more than 40 dams along the Douro), the terrestrial sediment input has been greatly reduced since the beginning of the 20th century, altering the sedimentary status of a significant part of the MDCs from depositional to erosional (according to unpublished AMS ¹⁴C dating results of surface sediment samples collected in the cruise). A large portion of the surface sediment sampled from the MDCs in the north (e.g., the Galician mud depocenter) is found to be remobilized from the MDCs in the south (e.g., the Douro mud depocenter) rather than being directly input by the rivers [e.g., Dias *et al.*, 2002a]. It thus becomes increasingly important to quantify the anthropogenic impact on the evolution of the MDCs and associated ecosystem. However prior to cruise M110 GALIMOS, the understanding of shelf hydrodynamics and sediment dynamics in this region was limited to the knowledge derived from the only observation that had been made through the European Union project Ocean Margin Exchanges (OMEX) [Vitorino *et al.*, 2002b]. During the OMEX cruises, the bottom-most monitoring instruments were placed 4–5 m above seafloor [Vitorino *et al.*, 2002b], too high to resolve the bottom boundary processes, especially those affected by the wave boundary layer, e.g., WCSTFs. Thus there exists still a gap in knowledge to link the real-time seafloor dynamics to the MDC development (Figure 1a) in this region, which may serve as a typical example for such processes.

3. Data Sets and Methods

3.1. Field Measurements

The GALIOMAR (Galician Ocean Margin) project was initiated in 2006 with the aim to investigate the stratigraphic framework of the continental margin of NW Iberia from the inner shelf to deep sea and comprised three cruises in the area by 2014 [Hanebuth *et al.*, 2007, 2012]. This project has developed a deep insight into the long-term evolution of MDCs (Figure 1a) and erosional zones on centennial to multimillennial time-scales [e.g., Lantzsch *et al.*, 2009, 2010; Schmidt *et al.*, 2010; Baasch *et al.*, 2014; Oberle *et al.*, 2014]. Based on the outcomes of these preceding cruises, the expedition M110 GALIMOS [Hanebuth *et al.*, 2015a] aimed at bridging the gap between short-term processes and long-term development of MDCs, with the goal to understand modern bottom sediment dispersal on the shelf driven by extreme external events.

Fifty-eight CTD profiles (42 stations), 8 particle camera imaging profiles, and 78 water samples were collected during the cruise to study the water column properties and vertical distribution of sediment. Twenty-eight Rumohr cores, 18 grab samples, and 7 gravity cores were collected to derive information on seafloor surface and subbottom sediment properties (e.g., grain size, composition, origin). Hourly-mean sea surface conditions (wind, current, wave, temperature, and salinity) were derived from two buoys. A sketch map of the cruise is shown in Figure 1b. For seafloor observations on the shelf, a lander mooring (Figure 1c) was equipped with three ECMs (Electromagnetic Current Meters) integrated with CTD (Conductivity, Temperature, Depth) and OBS (Optical Backscatter) sensors, an upward looking ADCP (Acoustic Doppler Current Profiler) 300 kHz, a downward looking ADCP 1200 kHz, and a LISST (Laser In Situ Scattering and Transmissometry). The lander was first deployed at a sandy site (73 m water depth) off the Douro river mouth from 16 to 20 September and in a second step in the center of the Galician mud depocenter (125 m water depth) off the Ría de Vigo from 21 to 26 September. During the first monitoring period, a storm that passed over the region was fortunately recorded (see supporting information Figure S1 and corresponding descriptions) and it led to the measurement of a 104 h time series recording the increase and subsequent decrease of storm-related energy conditions at the seafloor (as an analogue to the regime dominating during the winter season with prevailing westerly and southwesterly winds). The second monitoring period lasted for 109 h until a bottom trawler dredging incident. The instruments worked properly and data were successfully retrieved except for the top ECM and the downward looking ADCP 1200 kHz which malfunctioned. Two ROV dives were conducted near the sites of lander deployment to derive information of the seabed characteristics (bed form and bottom suspension observation, see supporting information).

3.2. Numerical Simulation

3.2.1. Model Description

A three-dimensional coastal ocean circulation model incorporating modules of sediment transport and sea-floor morphodynamics [Zhang *et al.*, 2012, 2014] is applied to the study area to investigate the storm-driven sediment transport across the continental shelf and its impact on the development of large-scale MDCs. The model was already successfully applied to wave-dominated coasts [Zhang *et al.*, 2014; Deng *et al.*, 2014] and bottom-current controlled deep-ocean sedimentary systems [Hanebuth *et al.*, 2015b; Chen *et al.*, 2016; Zhang *et al.*, 2016]. It couples some widely used models in a parallel computational structure to solve different processes. Through a module coupling interface, the model allows an integration of external functional modules to take into account specific processes of interest [Zhang *et al.*, 2013, 2015]. Major functional components of the model include:

1. A three-dimensional circulation-wave coupled module based on the Princeton Ocean Model [Blumberg and Mellor, 1987; Mellor *et al.*, 2008] adopting a fourth-order vertical pressure gradient scheme from McCalpin [1994];
2. A bottom boundary layer (BBL) module based on the Styles-Glenn model [Styles and Glenn, 2000] taking into account the impact of stratification induced by suspended particulate matter (SPM)—on the vertical structure of current velocity in the constant stress layer;
3. A subaqueous sediment transport module [Zhang *et al.*, 2010] modified from ECOMSED [HydroQual, Inc., 2002] for a process-based formulation of erosion, suspended load/bed load transport, and deposition of cohesive (one grain-size class) and noncohesive (multiple grain-size classes) sediment; and
4. A bathymetry update module based on the technique of morphological update acceleration and approaches for maintaining the computational stability [Zhang *et al.*, 2012].

The sediment transport module works on the same grid and coordinate system as the hydrodynamic module, meaning that the exchange of sediment between the seafloor and water column is calculated in the bottom-most layer of the sigma coordinate. In a coastal ocean model, the bottom-most layer is normally too thick to resolve the wave boundary layer that is restricted to several cm above the seafloor. To bridge the gap between the seafloor and the bottom-most grid point, the BBL module is used. Critical information in the Styles-Glenn model [Styles and Glenn, 2000] related to the calculation of (1) bottom shear stress due to the combined effects of currents and waves and (2) the vertical structure of the current velocity and SPM concentration in the constant stress layer is introduced in the supporting information. A detailed description of calibration of several critical parameters in the BBL module by field measurement and a coupling between the sediment transport module and the BBL module as well as model implementation of wave and current-supported gravity-driven sediment transport is also provided in the supporting information.

3.2.2. Model Setup for the Study Area

A nested grid system (Figure 2) was designed in order to provide a high-resolution simulation on the study area. A rectilinear regional grid with a uniform horizontal resolution of 4×4 km was used to provide open boundary conditions for a local grid focusing on the continental shelf with a horizontal resolution of 400×400 m. The bathymetry of the study area was generated based on the original bathymetric data obtained by high-resolution multibeam echo-sounder mapping during the GALIOMAR cruises. This local bathymetry was integrated into the latest GEBCO data set, which has a 30 arc-second resolution (GEBCO_2014, version 2014-11-03, <http://www.gebco.net>) to provide a regional bathymetry.

The regional model was divided into 20 vertical sigma layers with a uniform vertical resolution of $0.05D$, where D indicates the local water depth. The local model was divided into 30 sigma layers with a linearly increasing resolution from the sea surface ($0.05D$) toward the seafloor ($0.01D$). The minimum water depth was set to 20 m in order to ensure that the bottom-most grid point is located above u_{*c} , which is defined as the height (from the seafloor) of the upper boundary of a transition layer that is located between the wave-dominated region and the current-dominated region (see supporting information Text S5 for details). The driving forces for the model include the six major barotropic tidal constituents (M_2 , S_2 , N_2 , K_2 , K_1 , O_1) derived from TPXO 7.2 [Egbert and Erofeeva, 2002] with amplitudes corrected based on Quaresma and Pichon [2013], real-time winds (updated every 6 h) provided by Germany's National Meteorological Service (DWD), and the daily-mean river discharge from two major rivers in the region: the Minho River and the Douro River, provided through the online service of the Spanish (source: <http://www.chminosil.es/>) and Portuguese (source: <http://snirh.apambiente.pt/index.php?idMain>) authorities. A time-mean profile of salinity and temperature

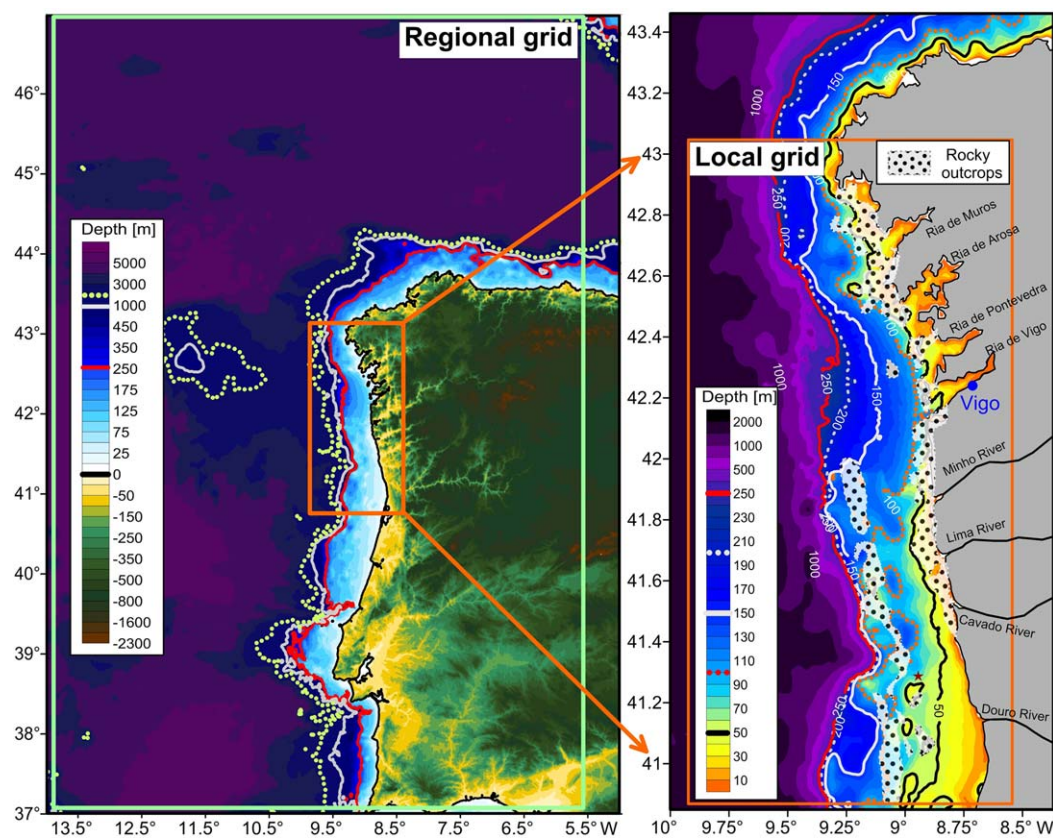


Figure 2. The computational grid system and bathymetry for the study area. Location of the lander mooring during the storm is marked by asterisk.

measured off the continental slope (2500 m water depth) in the beginning phase of the cruise (in between 14 and 15 September) was applied to the model domain as the initial thermohaline condition. Despite the occurrence of strong thundery rain showers during the storm, the discharge from the two major rivers remained relatively stable through the whole month (September 2014), between 75 and 200 m³/s at the Minho river mouth and between 100 and 360 m³/s at the Douro river mouth. The simulated tidal constituents and the water-mass flux, both taken from the regional model, were interpolated as open boundary conditions for the local model through one-way offline nesting. The inward variability from the open boundary to the interior local model domain was attenuated in a 10 cell wide sponge region. To ensure a better solution of surface gravity waves in the local model, parameters (wave height, period, and direction) of the two dominant wave bands derived from the lander mooring was added at the open boundary of the local grid as input.

The median grain size map of the seafloor surface sediment (Figure 1a) in combination with information from sediment cores (e.g., supporting information Figure S2) collected in all four GALIOMAR cruises was used to specify the composition of sediment on each grid cell. Sediment is categorized into five grain size classes according to the major mode composition of the grain size spectrum identified for the study area [e.g., Hanebuth *et al.*, 2007; Baasch *et al.*, 2014], with clay (0 to 4 μm , d_{50} = 2 μm), silt (4 to 63 μm , d_{50} = 40 μm), and very fine sand (63 to 125 μm , d_{50} = 100 μm) transported in the form of suspended load and fine sand (125–250 μm , d_{50} = 200 μm), medium sand (250–500 μm , d_{50} = 375 μm), and coarse sand (500–1000 μm , d_{50} = 750 μm) transported as bedload. The clay and silt classes are treated as aggregate-forming sediment which appear in the form of flocs. The real-time (i.e., time-dependent) settling velocities of the three classes transported as SPM are calculated from the constant settling velocities observed in still-water with additional effect of hindered settling (see supporting information Text S6 for details). The sediment resuspension/deposition rate is determined by a comparison between an equilibrium Rouse-like SPM concentration profile (supporting information S5–10) and the real-time profile that takes into account both diffusive

and advective transport (supporting information S6–6). Net deposition occurs when the amount of the real-time SPM concentration is in excess of the equilibrium value, otherwise net erosion would occur. A constant threshold for resuspension of the surface sediment (0.1 Pa) is used in the model, with an additional calibrating function describing the limit of sediment availability for resuspension due to consolidation and armor-ing effect (supporting information S6–11). This calibrating function is derived by a fitting of model result to observed near-bed SPM concentration during the storm. A spatially variable physical bed roughness length, which combines the Nikuradse sand grain roughness length and the form drag roughness induced by sand ripples or biological benthic structures observed in the field, is used to estimate the bottom shear stress due to combined effects of currents and waves (see supporting information Text S6 for details). The calculation of transport in suspension and as bedload is done independently without interaction between each other. It is worth to note that the impact by separating the calculation of bedload and suspended load from each other is minor since the mud depocenters mainly comprise silt particles.

The computational time steps in the local model are 90 s for the circulation module and 2 s for its internal (baroclinic) and external (barotropic) modes, respectively. For the sediment transport module and the BBL module, a time step of 120 s was used. The simulation period is from 00:00 UTC 1 September to 23:00 UTC 30 September. Since no measurement data exist for the vertical distribution of temperature and salinity before the date (14 September) when M110 cruise started, the model was set to operate on a diagnostic mode with temperature and salinity fixed before 00:00 UTC 15 September and on a prognostic mode since 01:00 UTC 15 September.

4. Results and Analysis

4.1. Field Data Analysis

Although the storm lasted for five days from 15 September to 20 September, its impact on the seafloor sediment dynamics was most remarkable from 16:00 UTC 16 September to 23:00 UTC 18 September as recorded by the lander. Afterwards the level of near-bed sediment concentration remained relatively low ($< 0.05 \text{ kg/m}^3$) and smooth. Based on this information, our following analysis will be focused on this 55 h time span.

The recorded time series of hydrodynamic conditions from a sea surface buoy (which is located on the continental slope off the Douro river mouth, see Figure 1b) and the lander instruments (ADCP 300 kHz and two ECMs) is illustrated in Figure 3. The local winds blow persistently from the south with a mean speed of 17 m/s, with wind gusts about 25 m/s in connection with heavy showers. Surface gravity waves were constrained in a narrow directional range between 240° (SW) and 290° (NW). Significant wave heights ranged between 3 and 4 m and maximum wave heights were about 6 m. The peak wave period alternatively switched between two narrow bands: 14–16 s and 9–11 s. Due to a strong wind drag the sea surface current was persistently poleward directed, and a semidiurnal tidal undulation was visible all through the water column, except for the sea surface for the first 15 h (i.e., from 16:00 UTC 16 September to 07:00 UTC 17 September). A complex circulation pattern is seen beneath 25 m water depth, suggesting that the midlayer and near-bottom current was to some extent decoupled from the surface current. Compared to a surface Ekman transport that is hardly recognizable at depths below 25 m, a bottom Ekman spiral is clearly visible in the midlayer and near-bottom current. Most remarkable in the time series are two periods of significantly enhanced current strength (named event hereafter), with one between deployment hours 3 and 4 (19:00–20:00 UTC 16 September) and the other between hours 13 and 14 (05:00–06:00 UTC 17 September). Hourly mean current velocity exceeded 20 cm/s at the seafloor in both events. Moreover, both events exhibit quite similar current patterns and they cannot simply be attributed to wind-driven or tidal transport.

Although of a similar mean current pattern, response of sediment resuspension to bottom current strength during these two events was quite different. High-resolution (4 Hz) time series of SPM concentration recorded by the turbidity sensors (OBS) of the ECMs and the grain-size composition of the SPM derived from the LISST data are illustrated in Figure 4. The mass concentration of SPM is derived by a calibration using the LISST data in combination with water and seafloor sediment samples collected in situ. Detailed information on the seafloor surface sediments sampled in the study area is given in the supporting information Text S2. For detailed technical treatments in the calibration, the reader is referred to the publically accessible cruise report [Hanebuth *et al.*, 2015a]. Although affected by a strong current with an

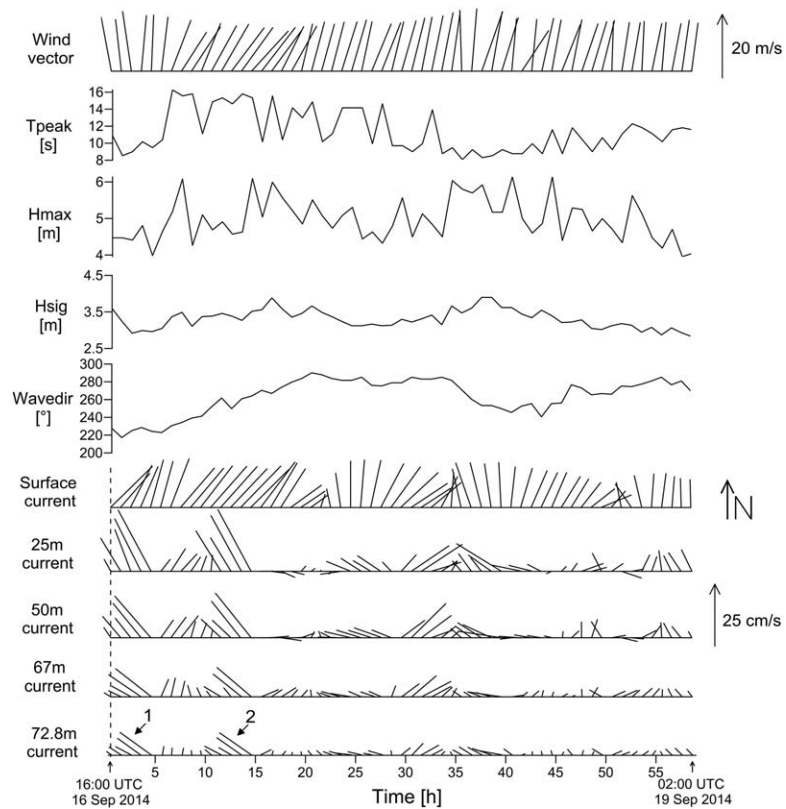


Figure 3. Monitored time series of hydrodynamic conditions (waves and currents) during the storm. Current data for 25, 50, 67 m is from the ADCP 300 kHz, and data for 72.8 m are from the bottom-most ECM. The ADCP data are vertically averaged over 5 bins (1 m/bin) centred at the depth indicated. The surface current and wave data are from the buoy. Note that the current data are hourly averaged. The two enhanced current events are marked as 1 and 2, respectively.

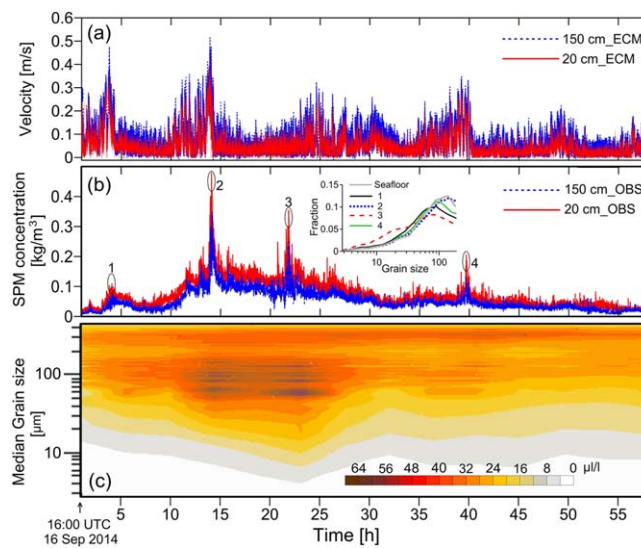


Figure 4. Monitored time series of (a) absolute current velocity, (b) mass concentration of SPM, and (c) grain-size composition (in terms of volumetric concentration of each grain size bin recorded by the LISST100) of the SPM. Spectra of SPM grain size during four suspension-enhanced events (marked by the numbers) and composition of local seafloor sediments are embedded in Figure 4b.

instantaneous velocity as high as 0.38 m/s (20 cm above seafloor), the recorded SPM concentration (30 cm above seafloor) did not exceed 0.1 kg/m³ during the first event. A significantly enhanced level of suspension, being five times higher than during the first event and almost two orders of magnitude higher than that in pre and poststorm periods, was recorded during the second event. The time lag between the maximum in current velocity (0.45 m/s) and the peak in SPM concentration (0.48 kg/m³) was 10 min during the second event. The minor difference in current velocity and remarkable difference in SPM concentration between these two events indicates that the local sediment resuspension was to a large extent governed by other forces rather than the mean bottom current strength. Another phenomenon

worthy of note is that although the current velocity decreased drastically after the second event and remained consistently below 0.2 m/s thereafter, the level of SPM concentration was persistently high in the following 15 h, showing even a second peak (marked by Number 3 in Figure 4b) between hours 21 and 22. This enhanced SPM concentration, which lasted for 21 h in total (from hours 10–31), was accompanied by a wide spectrum in SPM grain size composition. The combination of low current velocity and elevated SPM concentration after the second event suggests prolonged advective sediment transport at the seafloor. Grain-size distributions of mud particles (size less than 0.063 mm) in the SPM during suspension-enhanced Events 1, 2, and 4 are consistent with those of the local seafloor sediments (Figure 4b), suggesting that the increased portion of SPM during these events was mainly attributed to resuspension of local seafloor sediments. The SPM during Event 3 exhibited a clearly different grain-size distribution pattern with a significantly increased portion (18%) in the very fine class (size less than 0.03 mm), compared to the preceding events. The fining in sediment grain size in combination with a low shear stress during Event 3 indicates that the SPM mainly comprised sediment supplied from a remote source. Another phenomenon observed in the time series of SPM concentration particularly worth to note is a consistent signal of particles with apparent grain sizes larger than 0.2 mm. Granular sediments exceeding this size take up only a minor portion (< 4%) in the seabed composition at the monitored site, and they are commonly transported in the form of bed-load rather than as suspended load due to their high settling velocity. However, the consistently high volumetric concentration of these large particles through the entire monitored time span seems to contradict this fact. Such inconsistency provides us a strong argument to believe that the large suspended particles primarily consist of flocculated aggregates (“marine snow”) that drifted persistently in the water column during the storm. The ROV dive corroborated the presence of this “marine snow” showing a high floc density reducing the visibility to a few centimeter (see supporting information Figure S3).

To figure out the reason for the difference in SPM concentration among these events, especially between the first two events, the bottom-current data were decoupled into major periodic series according to those discernible driving forces behind them. As a first step the kinetic energy spectra of the current recorded in the bottom-most ECM was calculated to identify the major driving forces. Results show that two narrow bands of oscillations, one with a period ranging between 14 and 16 s and the other between 9 and 11 s, dominated the high-frequency (i.e., the band of wind-waves) spectrum. The 9–11 s band was predominant prior to the first event, while the 14–16 s band started to prevail with the beginning of the first event until 10 h after the second event. In both bands of oscillations, the west-east oriented component (u) dominated, suggesting that these waves’ crests were oriented almost parallel to the coastline at the site of the lander mooring. In the low-frequency time series (with periods larger than 5 min), the semidiurnal (M_2) tidal oscillation dominated, also with a predominant west-east oriented component. Based on the information of dominant periodic forces inferred from the kinetic energy spectra, the raw bottom-current data are filtered to sort out the amplitudes of these oscillations (Figure 5). First, the subtidal signal (with period T larger than 26 h) is derived by low-pass filtering (Butterworth) of the raw time series. Result shows the existence of a relatively stable northward-directed current with a velocity of 4 cm/s during the storm. The diurnal and semidiurnal tidal signals are subsequently derived by fifth-order band-pass Butterworth filtering of the current data in which the sub-tidal signal is removed. Cutoffs of each time series derived from band-pass filtering are indicated in Figure 5. The diurnal tidal current does not exceed 0.5 cm/s and thus its impact on the seabed sediment can be neglected. The semidiurnal tidal signal is, in contrast, notable and oscillated in-between ± 4.5 cm/s (positive sign for eastward direction) along the east-west axis and in-between ± 1 cm/s along the south-north axis (positive sign for northward direction), respectively. This result is consistent with existing studies on the characteristics of barotropic tides in the study area [e.g., *Quaresma and Pichon, 2013*]. After a removal of tidal and subtidal signals from the raw current data, time series of the major wind-wave motions are derived by band-pass Butterworth filtering. Results show that the 9–11 s wave band was relatively stable, mostly oscillating in-between ± 8 cm/s and episodically enhanced to maximum of ± 11.5 cm/s, while the 14–16 s wave band was quite variable, with an increasing orbital velocity during the first 14 h and a decreasing trend thereafter. Most notable variation in the 14–16 s wave band is a drastic increase in orbital velocity between hours 13 and 14 coinciding with a drastic increase in the mean current velocity (Figure 5), suggesting an enhanced wave-current interaction that resulted in the second energetic event. This event is different with the first event which was driven mainly by the mean bottom current. The wave-current interaction induced a significantly enhanced level of sediment resuspension compared to that produced by a mean current of comparable magnitude alone [e.g., *Grant and Madsen, 1979*].

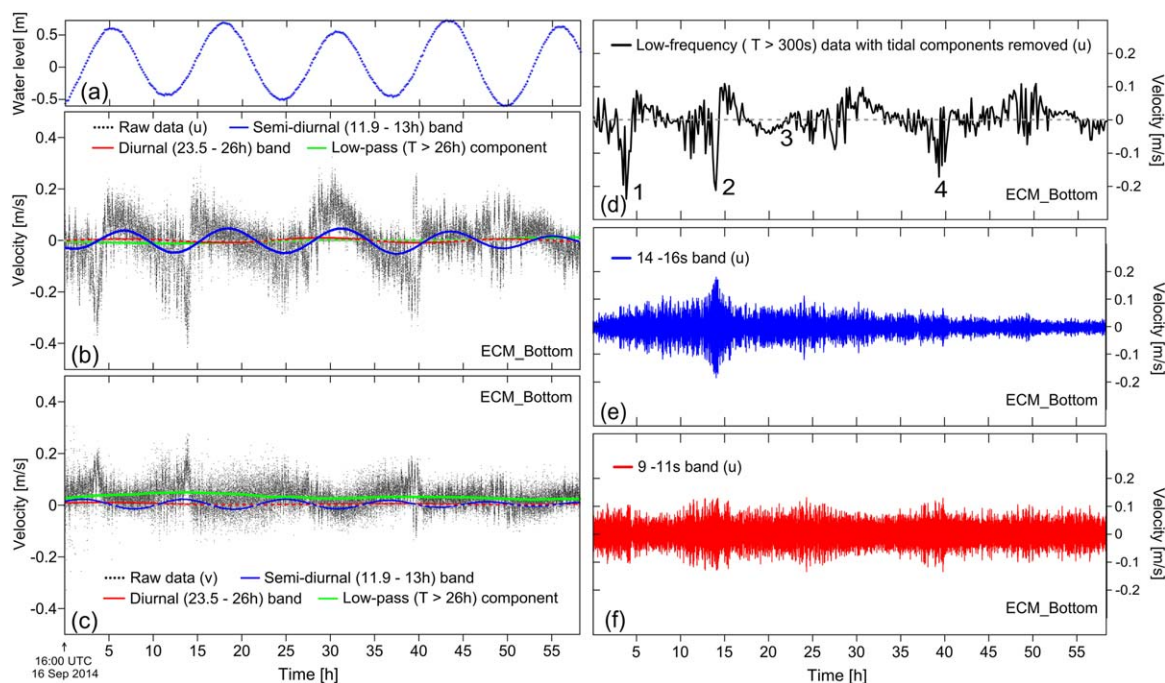


Figure 5. (a) Time series of water level at the site of the lander mooring inferred from pressure sensors. The west-east oriented component (u) and the south-north oriented component (v) of the raw current data recorded by the bottom-most ECM (20 cm above seafloor) are plotted in (b) and (c), respectively, together with their low-frequency constituents. (d), (e), and (f) show the major constituents of the west-east current component after a removal of tidal constituents. The nonperiodic motions corresponding to the four suspension-enhanced events are also marked in Figure 5d.

Although the periodic motions accounted for the bottom-current variability to a large extent, an undulation by nonperiodic forces existed during the storm and was especially remarkable during Event 1, 2, and 4 (Figure 5d). Maximum current velocity associated with nonperiodic forces exceeded 20 cm/s in the first two events with a predominant west-east oriented component. The nonperiodic motions in the first two events showed a quite similar pattern, with a west-east oriented component (u) directed inversely in a short period (20 min) after reaching the peak value. It is difficult to discern the exact driving mechanism for these nonperiodic motions simply from the monitored data. One particular phenomenon related to Event 1, 2, and 4 is that the sea-surface temperature decreased during these events, while an accelerated increase in temperature was observed at the seafloor (Figure 6). The seafloor temperature continued to rise for a short period (0.5 h) after both events, and then remained stable for about an hour. Afterward it slowly dropped back to the general level shown during the event and remained relatively stable for several hours. This particular temperature variation, which exhibits a core of warm water, in combination with a drastically inverted current direction after both events implies a possible transit of oceanic density fronts at the mooring site. In order to evaluate such a scenario as a major driving mechanism during both high-energy current events, with particular emphasis on the second event that initiated a long-lasting (21 h) advective sediment transport on the seafloor, it is necessary to carry out a high-resolution three-dimensional numerical simulation of shelf dynamics driven by the storm. Our intention is also to derive a comprehensive picture of the hydrodynamics and sediment transport on the continental shelf induced by such events.

4.2. Model Results and Analysis

After calibration of the BBL module and near-bed sediment transport module by field data, the 3-D model is applied to simulate the storm impact on the entire shelf. A comparison between simulation results and measured field data shows a satisfactory model performance (demonstrated in Figure 6). Comparison between model results and field observation is done at a large spatial scale, including at two lander deployment sites (locations indicated in Figure 1b), two surface buoys, two tidal gauge stations (the lander and a fixed station in Vigo, see Figure 1b), and various CTD stations on the shelf. Root Mean Square Error is calculated to evaluate the model performance. The simulated tides are consistent with the measured data derived

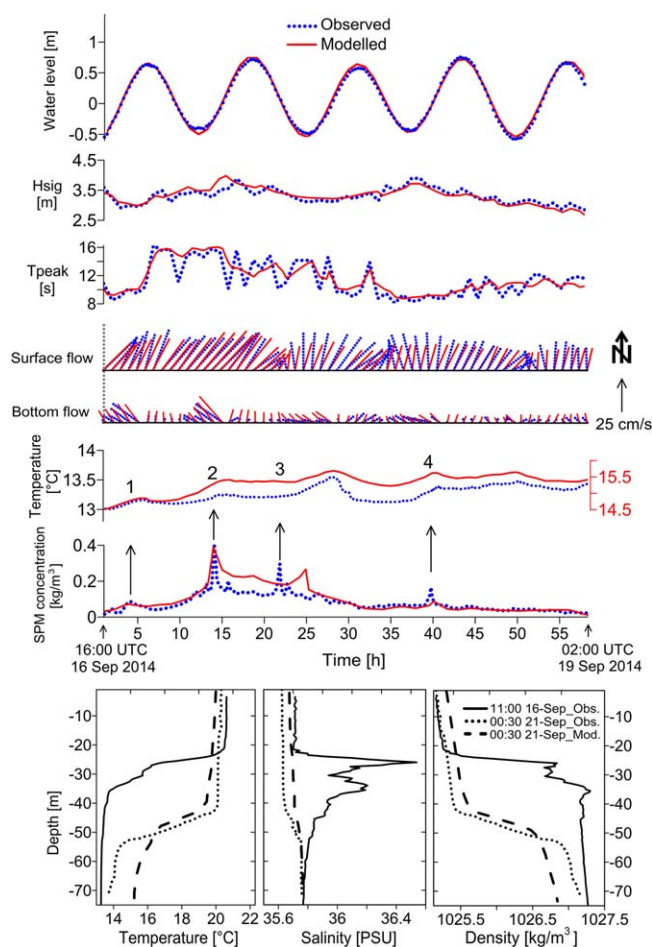


Figure 6. Comparison between observed data and simulation results at the first lander monitoring site and at a CTD station (location marked as 04 in Figure 1b). Temperature variation during four suspension-enhanced events is marked by numbers.

After the pass of the storm, hydrodynamic conditions at the second deployment period were characterized by poststorm relaxation and dominated mainly by tides, which are also satisfactorily reproduced by our model result. During the relaxation, settling of sediment occurred. This was reflected by a constantly low level of near-bed SPM concentration recorded by the lander [Hanebuth *et al.*, 2015a]. The overall good agreement between simulation results and field data provides us a strong argument that the model has reliably reproduced a complete 3-D scenario of hydrodynamics and morphodynamics in the entire shelf system driven by the storm and that the results can thus be interpreted in further detail to derive insights into the driving mechanisms for the bottom sediment transport.

4.2.1. Hydrodynamic Conditions During the Storm

Measured vertical profiles of water properties on the midshelf (60–100 m water depth) before the arrival of the storm front showed a remarkable difference in temperature (by $\sim 10^{\circ}\text{C}$) and a minor difference in salinity (by 0.16 psu) between surface and bottom waters [Hanebuth *et al.*, 2015a]. The difference in temperature and salinity resulted in a density difference as large as 2.2 kg/m^3 between the warm surface water and the cold bottom water on the midshelf. The thermohaline pycnocline was located between 20 and 35 m water depth before the storm. Measured winds from 1 to 15 September were relatively weak and oscillated between 0.4 and 8 m/s with an in general increasing trend and a prevailing southerly direction. Significant wave height measured by the buoys in September did not exceed 3 m before the arrival of the storm. Starting from 02:00 UTC 16 September wind speed increased rapidly and reached 16 m/s at 07:00 UTC 16 September with gust up to 25 m/s. A transient calm period with wind speed of 9 m/s appeared between 14:00 and 17:00 UTC 16 September and enabled a deployment of the lander. Afterward the wind strengthened

from the lander and gauge station in Vigo, with a RMSE of 0.03 m in the amplitude and 0.8° in the phase. With the parameters of two dominant wave bands (derived from the lander) added to the open boundary the simulated wave parameters are in good agreement with the buoy data, with a RMSE of 0.11 m in the significant wave height (H_{sig}) and 0.85 s in the peak wave period (T_{peak}). The two strong current events (i.e., Event 1 and 2) were successfully reproduced by the model, despite of an angle deviation of 19° between the modeled and the measured data. The temporal and spatial variation in temperature and salinity at the lander mooring site during the storm is also reflected in the model results (Figure 6), though the modeled temperature is 2°C higher than the observed data. A depression of the thermohaline pycnocline induced by the storm is clearly seen in both the observational data and the model result. Sediment resuspension and transport, especially during the second event and the following 17 h period of active advective transport, was successfully reproduced by the model, despite of a time lag of 3 h between the simulation results and the field data for the appearance of the third suspension enhanced event (Figure 6).

again and persistently ranged above 12 m/s until 20 September. The strong southerly winds accompanying the storm front effectively drove the surface mixed water toward the coast. Modeled sea surface current on the outer shelf was directed north-eastward with an angle of 20° deviated from the wind direction and gradually tuned to run parallel to the coastline on the inner shelf. The strength of the surface current increased from 0.15 m/s on the shelf edge to 0.8 m/s in shallow coastal areas (Figure 7).

The modeled onshore-directed Ekman transport driven by the winds was prominent in the outer and mid-shelf surface water with a thickness of 30 m (Figure 8). The build-up of water at the coast resulted in an across-shelf water level gradient as large as 7×10^{-3} m/km and led to pronounced downwelling of surface waters. The modeled offshore-directed bottom flow lowered the pycnocline and pushed it offshore, leaving behind an inner shelf region where water density was vertically well mixed (Figures 7 and 8). Due to a large density difference between the surface and bottom waters, a strong positive buoyancy was generated at the interface between the downwelling water and bottom water, producing a vertical density front and a region with a significantly increased across-shelf density gradient (Figures 7 and 8). In the initial phase (first 5 h) of the storm-induced downwelling, the density front was developed in shallow waters and its structure was more pronounced in the southern part of the study area (i.e., south of the Minho River) where the across-shelf bathymetric slope was milder than the northern part of the area. Continuous downwelling drove the front offshore in the south and facilitated a development of the front in the northern part of the study area at the same time. The front structure in the density field was easily recognizable and concentrated near the seafloor (Figures 7d and 8a), while the front structure in the current velocity field exhibited a complex spatial pattern (Figures 7b and 8c, 8d). A strong, surface-intensified alongshore coastal jet formed in the shoreward vicinity of the front and extended over the full water column. Alongshore current velocity in the jet near the sea surface approached 0.4 m/s in the initial phase of the storm, and increased up to 0.7 m/s as the downwelling front migrated offshore. The front contained a downward vertical motion from the sea surface to the seafloor with velocities up to 0.4 cm/s. Just seaward of the front an upward vertical water motion developed with velocities up to 0.2 cm/s. An upward motion occurred shoreward of the front as well, but of very weak intensity (0.02 cm/s).

The flow converged at the seaward edge of the front and diverged at its shoreward edge, with a strong offshore component (up to 0.25 m/s) inside the front and a weak onshore component (several cm/s) in the vicinity of its both edges. These front-associated flows constituted secondary circulations in the shelf transport system and involved temporal and spatial fluctuations in their intensity as the front migrated. Inside the front the water temperature was slightly higher than in the surrounding area due to a downward vertical motion of surface waters. At the same time the surface water above the front became cooler than in the surrounding areas due to an upward vertical motion of water from the seafloor at the front edge. The modeled increase in temperature inside the front and decrease at the front's edges provide a sound explanation for the temporal variability observed by the lander (Figure 6), and suggest that the periodic-like increase in temperature in the observed time series corresponded to the arrival of the front at the lander site.

Model results indicate that due to variations in the wind stress and tidal undulation, the location of the front oscillated during the storm, with an amplified range in the southern part of the study area where the lander was located. The first arrival of the front at the lander site was responsible for the first strong current event. However, the front drew back inshore due to a weakening of the downwelling which resulted from a weakening of surface wind stress, with a time lag of 4 h. In the following 6 h period, the bottom current at the lander site was quite weak (2–5 cm/s) and exhibited an (1–3 cm/s) onshore transport component (Figure 6). After this calm period, the arrival of the second front at the lander site and its interaction with swells (14–16 s) induced the second strong current event. The wave-current interaction resulted in a bed shear stress as high as 1.76 Pa at the lander site and induced massive local resuspension of fine sediment particles according to model results. After the second event the front drew back inshore again and exhibited a 12 h cyclic period in its appearance at the lander site (Figure 6), suggesting a semidiurnal tidal control of its across-shelf oscillation.

4.2.2. Bottom Sediment Transport During the Storm

The simulation results indicate that the resuspension of seafloor sediment in the initial phase of the storm was restricted to shallow water with a northward increasing impact depth from 70 m off the Douro river mouth to 90 m off the Minho river mouth. No seafloor sediment resuspension occurred north of 42° latitude except inside the Spanish rias (i.e., the drowned river valleys in the northern part

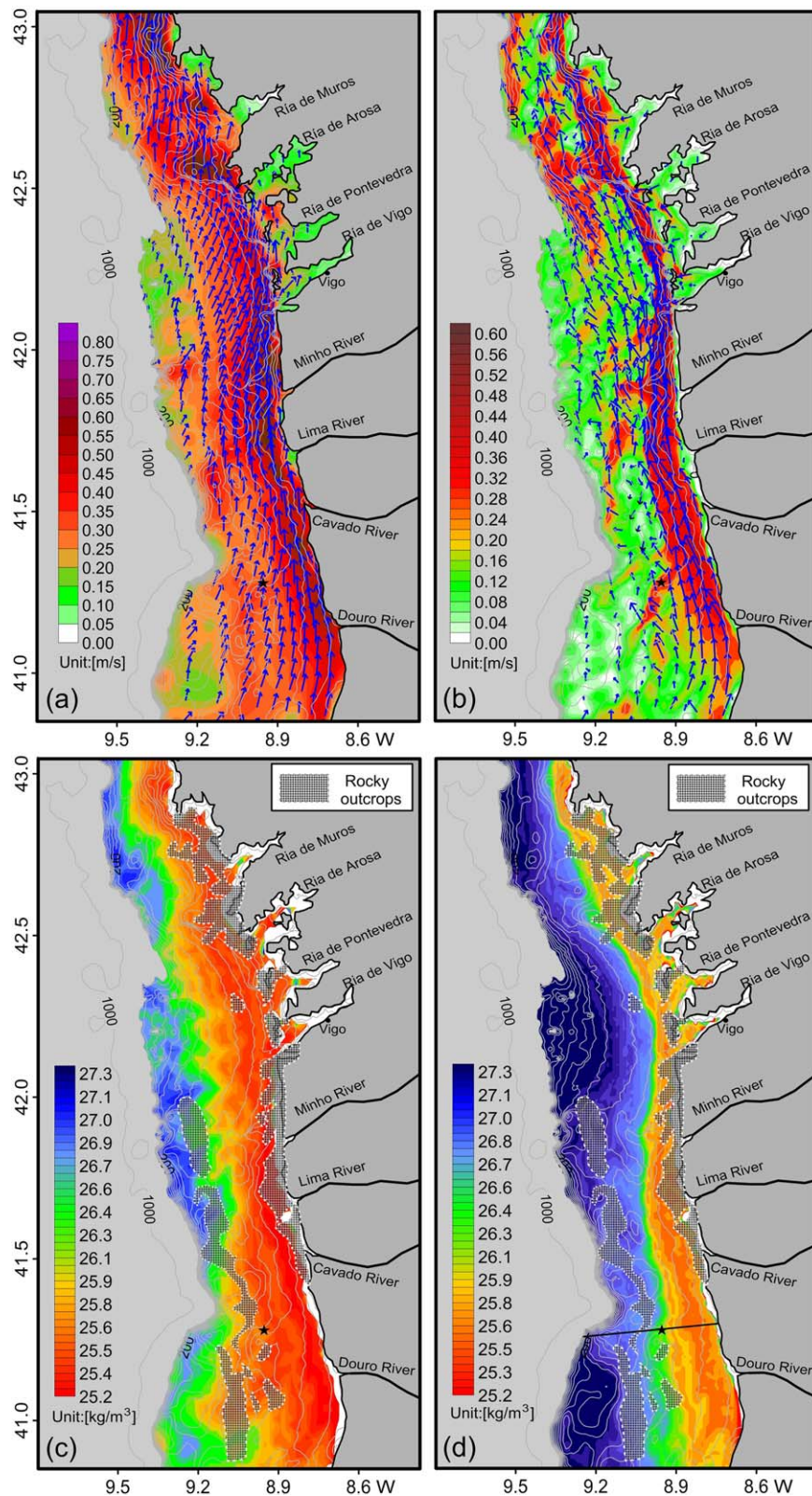


Figure 7. (top) (a) Simulated surface and (b) bottom current fields during the second event. Vectors are plotted over eight grid cells in both x and y direction. (bottom) (c) Simulated surface and (d) bottom water density fields during the second event. The site of lander mooring is marked by asterisk. An across-shelf profile, which is plotted in the following figure, is marked by the solid line in Figure 7d.

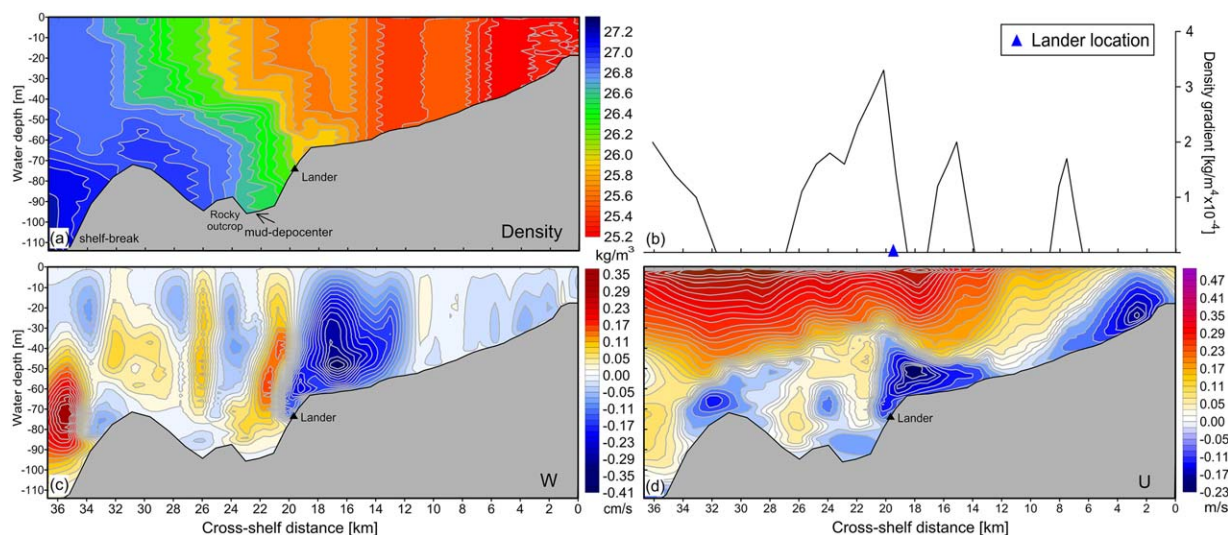


Figure 8. Simulated across-shelf distribution of (a) water density, (b) density gradient, (c) vertical current velocity, and (d) west-east oriented current velocity during the second event.

of the study area that show an reduced opening to the sea and experience minor river discharge) due to the exceptionally great water depths on the shelf of more than 100 m in the immediate seaward vicinity of the mouths of the rias. Maximum near-bottom SPM concentration appeared near the Douro and the Lima river mouths with values up to 0.5 kg/m^3 at 20 cm above seafloor. As the oceanic density front further developed and migrated offshore the area of sediment resuspension expanded toward deeper waters. Due to a downward water motion in the coastal jet as well as in the front suspended particles were mostly restricted near the seafloor and their transport was controlled not only by a strong northward current in the coastal jet but also by secondary circulations such as flow convergence and divergence associated with the front. As a result patches of elevated levels in SPM concentrations, with values up to 0.75 kg/m^3 at 20 cm above seafloor, formed in the flow convergence zone as well as in the coastal jet after the initial phase (5 h) of the storm. The location of the front stabilized laterally after the second event except for a secondary undulation imposed by tides that oscillated within 2 km from its seaward-most point. A comparison between the front location during and after the second event and the shoreward boundary of the MDC nucleus (with mud content exceeding 80%) indicates a geographic coincidence between them (Figure 9), suggesting the primary control of the front on transport and deposition of fine-grain sized sediment on the shelf. In the vicinity of the seaward edge of the front, bottom currents were very weak and exhibited an onshore direction. The weakening in current strength in combination with the flow convergence allowed for an accumulation and deposition of SPM at the seaward side of the front, eventually forming the nucleus of the MDCs. It is worth to note that the topographic relief associated with the rocky outcrops on the outer shelf in the southern part of the study area plays an important role in constraining a seaward expansion of the MDC. These rocky bedrocks are several meters high and act as a barrier widely hindering offshore sediment dispersal. As a result, the dimension of the MDCs in the southern part of the study area is restricted to the area between the front-impact zone and the rocky outcrops.

Interaction between the surface gravity waves (14–16 s band) and strong bottom currents associated with the front led to massive resuspension of seafloor sediment during the second event (Figure 10). According to the simulation results near-bottom (20 cm above the seafloor) SPM concentration exceeded 0.25 kg/m^3 in a major part of the shelf and high levels of near-bottom SPM concentration exceeding 10 kg/m^3 occurred at some muddy places. These sites of high-level near-bottom sediment concentration were laterally scattered and mostly initiated in association with flow convergence. Model results indicate that the maximum SPM concentration in these suspensions exceeded 25 kg/m^3 (e.g., Figure 11a) and they can be categorized into two different types with regard to their formation mechanism. The first type (Type I) was generated inside the coastal jet by a combined effect of strong wave shear stress and strong current shear stress. An example of this type is shown in Figure 11b.

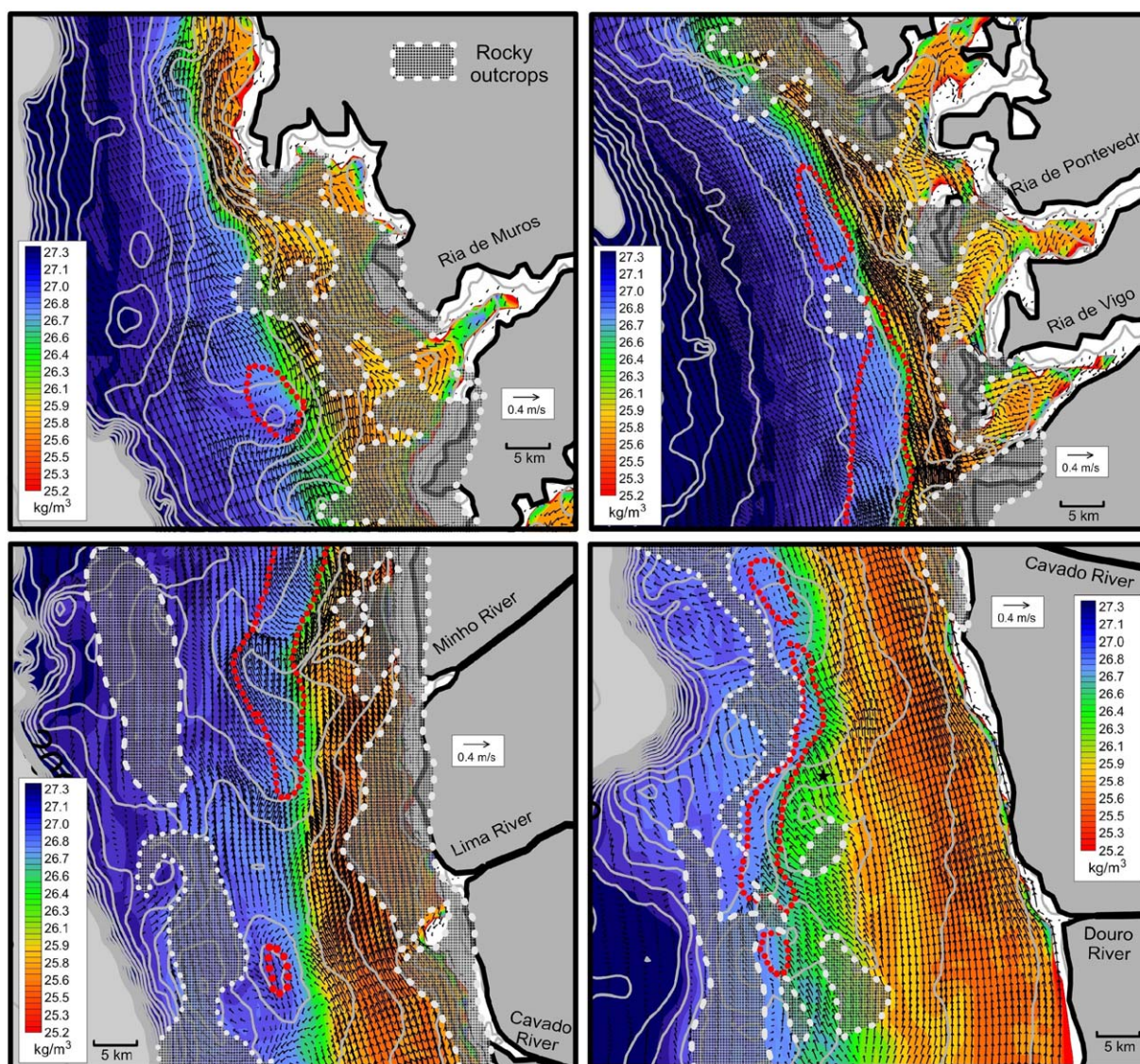


Figure 9. Simulated current (arrows) and water density (color) fields in the bottom-most layer during the second event. Current vectors are plotted over two grid cells in both x and y direction. The seaward edge of the storm-generated downwelling front coincided with the shoreward boundary of the nucleus of MDCs (indicated by dashed frames) where mud content exceeds 80%.

The bed shear stress induced by an enhanced wave-current interaction was as high as 3.6 Pa at this site and resulted in local sediment resuspension with concentrations exceeding 18 kg/m^3 within a layer of 5.4 cm (z_1) above the seafloor. The second type (Type II) was initiated by a strong wave shear stress on a muddy seafloor and enhanced by a convergence in sediment transport flux in the frontal zone. An example is shown in Figure 11a. The maximum wave shear velocity at this site during the second event was 4.7 cm/s, which is comparable to that (5 cm/s) at the exemplary site inside the coastal jet. However, the maximum current shear velocity was 1.4 cm/s here, being significantly lower than that (3.5 cm/s) at the site inside the coastal jet. The difference in current shear velocity between the two types of suspension resulted in different profiles with regard to the gradient Richardson number in the wave boundary layer (Figure 11). The Richardson number of the Type II suspension is much larger than 0.25 (i.e., the threshold for occurrence of WCSTFs, see supporting information Text S7), suggesting a significant downslope gravity-driven transport component, while the Richardson number of the Type I suspension is much smaller (although still exceeding the threshold) compared to that in Type II. In this case the transport of Type I suspensions was controlled mainly by the mean-current. Simulation results indicate that the very fine sand class (63–125 μm) contributed to a significant

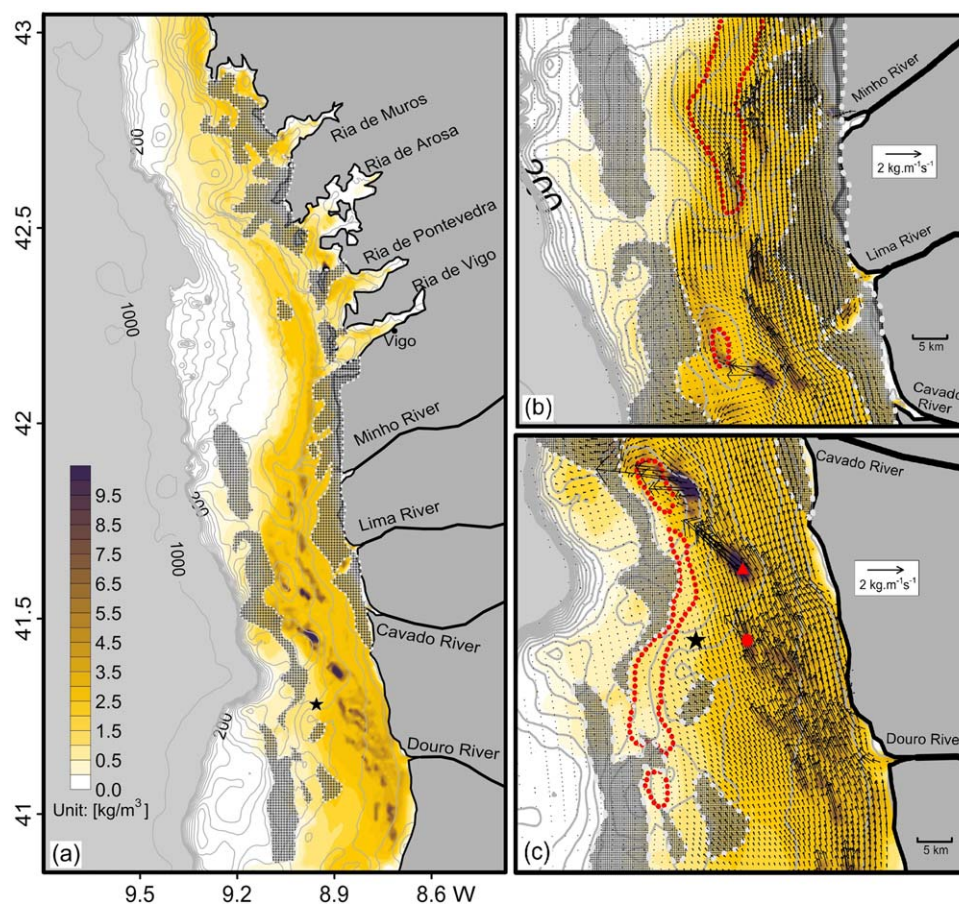


Figure 10. Simulated SPM concentration at 20 cm above the seafloor during the second event. The arrows in (b) and (c) indicate the vectors of the sediment transport flux in the bottom-most 0.5 m. These vectors are plotted over two grid cells in both x and y direction. The site of lander mooring is marked by asterisk. Vertical profile of SPM concentration at two sites, which are marked in (c) by triangle and circle, respectively, is plotted in the following figure.

portion of the SPM inside the wave boundary layer and its concentration decreased drastically above the wave boundary layer, while concentration of the mud classes exhibited a milder vertical gradient near the seafloor. Settling velocity of sediment particles was significantly reduced in the highly concentrated suspensions due to a hindered settling effect (see supporting information Text S6). The reduction (by more than 40%) of settling velocity played a major role in maintaining these suspensions after the second event according to simulation results.

Simulation results also indicate that the third suspension-enhanced event during hours 21–22 (Figure 4) is attributed to the residual effect of highly concentrated suspensions that occurred in the upstream area, despite a 3 h lag in appearance of this suspension in the simulation results (Figure 6). It should be noted that highly concentrated near-bottom suspension was not directly detected by the lander. The maximum SPM concentration at the lander site did not exceed 2 kg/m^3 (see supporting information Text S6). However, based on a calibration of the BBL model using the observational SPM data and the good agreement between the simulation results and spatial field data, we have the confidence to believe that highly concentrated near-bottom suspensions occur during such energetic event. A model run excluding SPM-induced stratification effect and gravity-driven transport failed to reproduce the third suspension-enhanced event. The SPM-induced stratification effect plays a critical role in constraining the high-level SPM concentration within a thin layer above the seafloor according to our model results. Without this effect the modeled SPM concentration at a height of 10 m above the seafloor was as high as 0.5 kg/m^3 at various muddy sites during the second event (Figures 11a and 11b). Such high value does not fit our field measurements which indicated that the SPM concentration at 10 m above the seafloor did not exceed 0.01 kg/m^3 over the shelf during the storm [Hanebuth et al., 2015a].

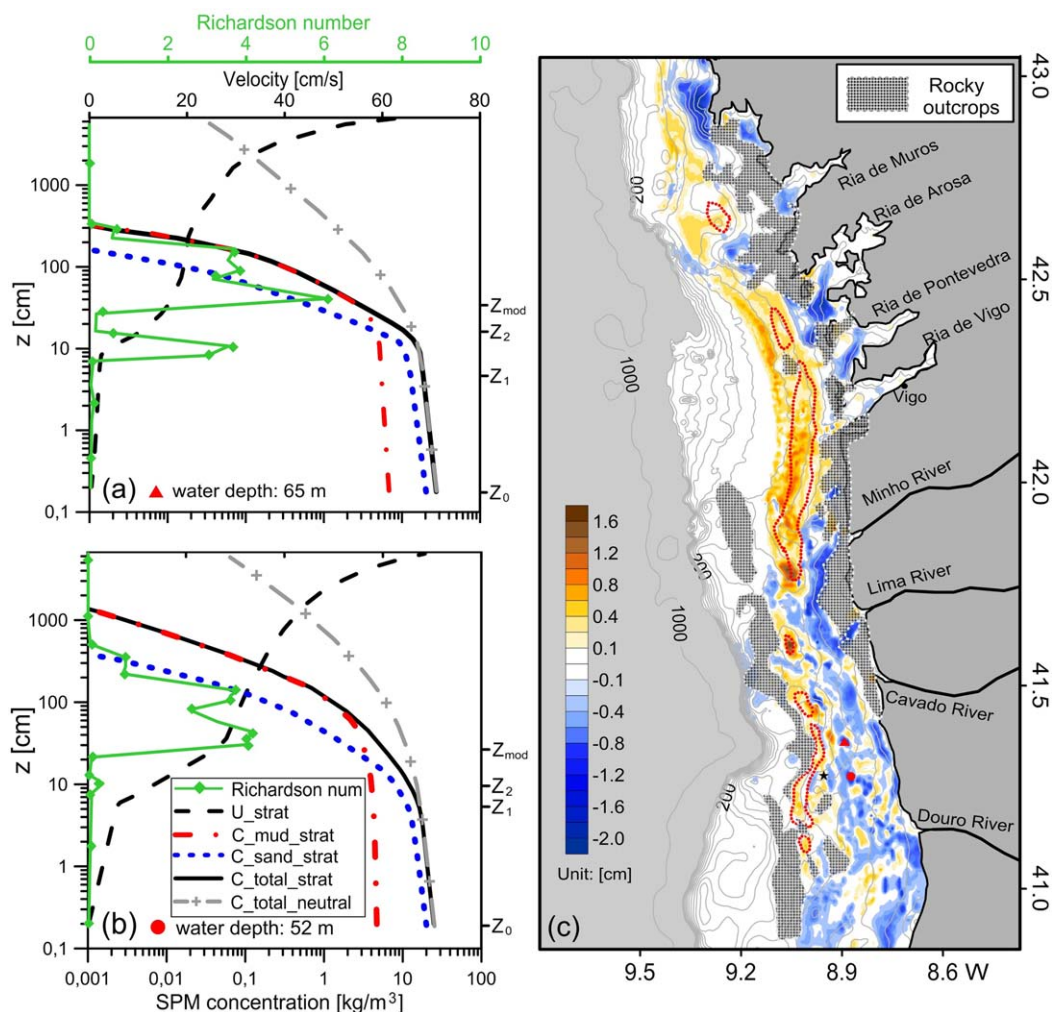


Figure 11. (a) and (b) Simulated vertical distribution of SPM concentration (including results with and without SPM-induced stratification effect), mean current velocity affected by stratification (U), and gradient Richardson number (R_i) during the second event at two exemplary sites. (c) Simulated bottom elevation change at 720 h. Positive and negative values indicate depositional and erosional thickness, respectively. Locations of the two exemplary sites of high-level SPM concentration inferred by model result are marked in Figure 11c.

The modeled bed elevation change at 720 h (i.e., at 23:00 UTC 30 September) indicates widespread erosion on the shallow shelf as well as significant deposition on the existing MDCs (Figure 11c). The maximum depositional thickness (1.6 cm) exactly takes place in the nucleus of the MDCs and is associated with settling of near-bottom concentrated sediment suspensions (Figure 10). Simulation results also indicate that deposition on a major part of the MDCs is attributed to a settling from dilute suspension in the BBL (Figure 10a).

5. Discussion

A good agreement between the measured field data and numerical simulation results demonstrates the robustness of an elaborate 3-D coastal ocean model for studying storm-driven bottom sediment transport on the continental shelf. Our study area, i.e., the NW Iberian continental shelf, represents a typical high-energy narrow shelf setting which is subject to frequent seasonal storm impacts. Deposition of fine grained sediment is not straightforward in such energetic environment, despite the fact that numerous large-scale mud depocenters are found in this area. Thus, the key to understand the formation of large-scale sedimentary systems in high-energy continental shelf environment is to figure out how fine grained sediment is transported and allowed to deposit on the seafloor during energetic events, e.g., storms. To answer this question field monitoring and seabed surveying in combination with high-resolution process-based

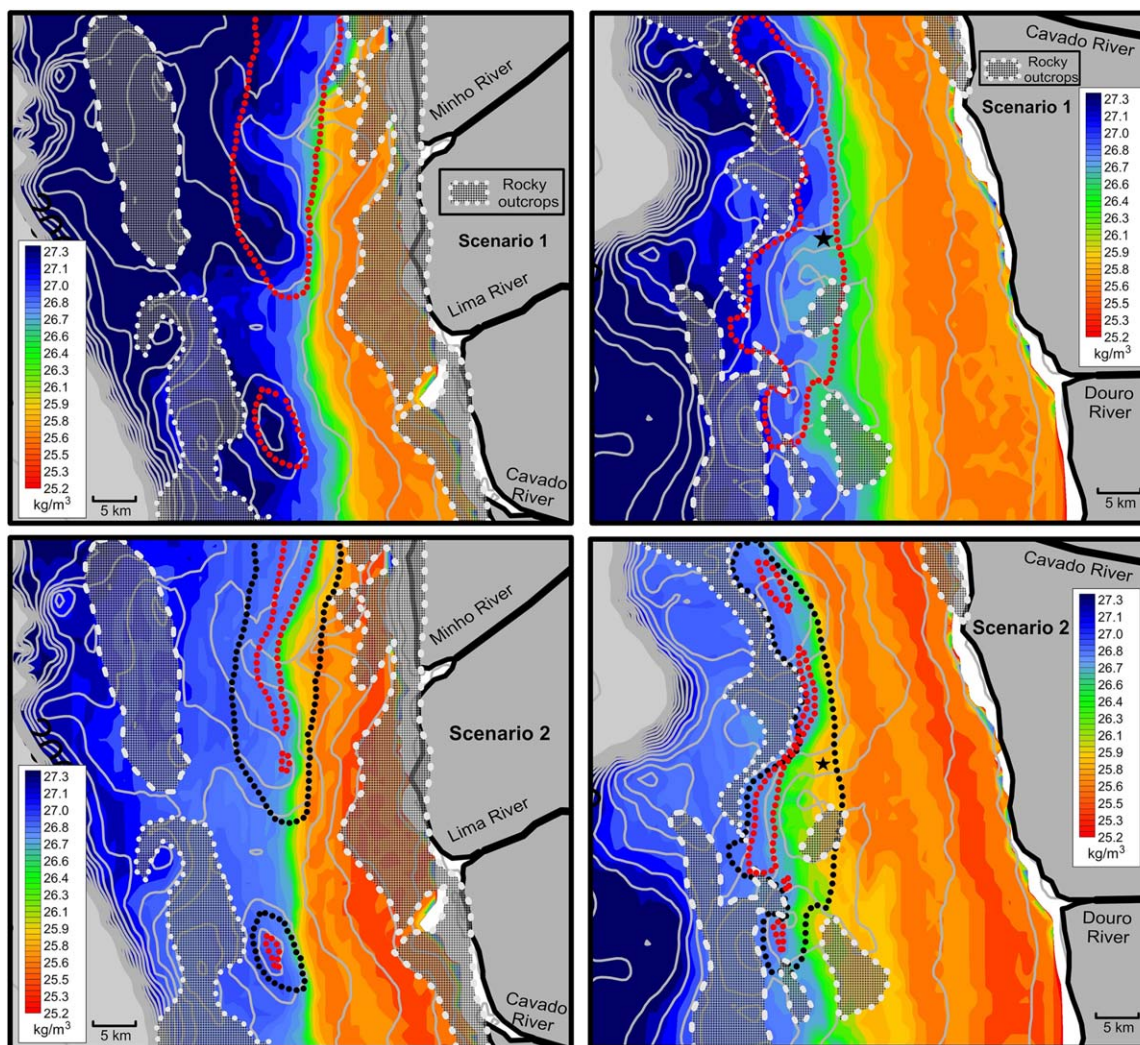


Figure 12. Simulated bottom water density fields during the second event for scenarios of 30% decreased (Scenario 1) and 30% increased (Scenario 2) wind strength with reference to the observed data. The red-dashed polygons in Scenario 1 indicate the area where mud content exceeds 45%, while those (red dashed) in Scenario 2 indicate the area where mud content exceeds 90%. For an easy comparison, the dashed polygons in Scenario 1 are also indicated in Scenario 2.

modeling provides the optimum method. It has been found that the inner and midshelf hydrodynamic system in the study area is mainly driven by tides and wind-forced currents and largely decoupled from those large-scale ocean circulations which prevail off the shelf edge along the Iberian margin [e.g., *Csanady and Shaw, 1983; Relvas et al., 2007*]. This decoupling allowed us to exclude the large-scale circulations in the simulation and to focus on the impact of winds and waves on bottom sediment transport. A good agreement between the simulation results and field measurement data further proves such decoupling of processes and provides a sound explanation on the formation and development of MDCs.

Simulation results from this study show that two means of near-bottom transport, i.e., dilute suspension in the Bottom Boundary Layer (BBL) and concentrated sediment suspensions in the wave boundary layer, are the dominant patterns of across-shelf sediment transport and are responsible for formation of MDCs. WCSTFs are not responsible for deposition on a major part of MDCs, but they seem to contribute to the maximum deposition at several MDCs. Since WCSTFs on gently sloped shelves are triggered by extreme wind-wave conditions and their formation results from a combined effect of several processes, it requires fortunate circumstances to capture such processes in field, and the scarcity of field data limited our progress in a quantitative understanding of the 3-D structure of WCSTFs and their migration on the seafloor. Our approach to simulate WCSTFs is largely based on the validity of the Styles-Glenn model [Styles and Glenn, 2000]. By the use of relatively simple empirical formula to parameterize the vertical structure of

near-bed SPM concentration and its impact on current velocity the model is computationally efficient in resolving a high-resolution structure of near-bed SPM and current velocity. Despite of a wide use of the Stiles-Glenn model in community models [e.g., Warner *et al.*, 2008], laboratory experiments [e.g., Herrmann and Madsen, 2007] and field studies [e.g., Allison *et al.*, 2005], potential errors in the formulation, e.g., application of Newton's law of viscosity (supporting information S5-1) to highly concentrated sediment suspensions (e.g., fluid mud) where the sediment-water mixture behaves more like non-Newtonian, have not been evaluated yet. More effort is thus required to explore the applicability of our approach to different coastal and marine environments.

The coincidence between the seaward edge of the storm-generated downwelling front and the shoreward boundary of the nucleus of MDCs (Figure 9) suggests a clear physical link between these two elements, despite the fact that they evolve on quite different temporal scales. One might argue that the front location might be variable under different boundary conditions (e.g., strength of the storm) and does not necessarily always coincide with the nucleus of MDCs. In order to test the spatial variability of storm-generated downwelling fronts in the study area, an additional set of model runs was carried out in which the two critical parameters, i.e., the initial density difference between surface and bottom waters and the wind strength during the storm, were tuned in a certain range ($\pm 30\%$) from the reference (i.e., observed) data. Results indicate that the downwelling front generally locates shallower when the wind strength is weaker (Figure 12). The geographic location of the front, however, becomes more or less stabilized along with an increase in wind strength above the reference level (Figure 12). An increase of the wind strength by 30% induces a vertically extended front impact depth deeper by only less than 5 m compared to the reference data. On the other hand, the structure of the front and the coastal jet becomes less prominent when the initial density difference between surface and bottom waters decreases. As an extreme case in the designed scenarios, a strengthening of the wind strength by 30% in combination with a weakening of the vertical density stratification by 30% reduces the cross-shelf horizontal density gradient at the front by 60%, leading to a weakening of the coastal jet (maximum current velocity reduced by 25%) and a strengthening of offshore transport (current velocity increased by 30%) seaward of the front due to a barotropic effect. This scenario results in a deeper depositional area mainly to the north of the Lima river for fine grained sediment, approaching the very nucleus of the MDCs where mud content exceeds 90%. Results of these scenarios suggest that strong storms acting on strongly stratified shelf waters provide the optimum condition for the development of MDCs in the study area. In this sense, the first storm after the summer season, when the temperature difference between the surface and the bottom water reaches a peak value, should play the most important role among all storms occurred in winter season in facilitating the formation and development of MDCs.

6. Conclusions

Through an integrative study that combined field monitoring, seabed surveying, and numerical simulation, we investigated how a downwelling-favorable storm drove bottom sediment transport on the NW Iberian continental shelf and its relationship with the large-scale formation of midshelf mud depocenters (MDC) in this region. Three major conclusions are drawn from this study. First, the storm-generated downwelling front and associated coastal jet impose a primary control on transport and deposition of fine-grained sediment on the shelf. The shoreward boundary of the centers of the MDCs can be regarded as a geographic marker for the offshore limit of the downwelling fronts, vice versa. Second, simulation results indicated that such energetic event is able to produce near-bottom sediment suspensions with concentrations of the order of 10 kg/m^3 in various muddy areas of the shelf. These concentrated sediment suspensions can be categorized into two types owing to a difference in the gradient Richardson number in the wave boundary layer. Type I is generated inside the coastal jet by a combined effect of strong wave shear stress and strong current shear stress and transported mainly by the mean current, while Type II results from strong wave shear stress in the frontal zone in combination with convergence in sediment transport flux and is characterized by a significant gravity-driven transport. Storm-driven transport and post-storm deposition of these concentrated sediment suspensions should have a direct consequence for several MDCs. Finally, our study emphasizes the need for a high-resolution representation of near-bottom SPM transport in existing coastal ocean transport models. This inclusion is critical in understanding dispersal of fine-grained sediment and morphogenesis of large-scale mud depocenters in high-energy continental shelf environments.

Acknowledgments

We would like to express our great gratitude to Captain Rainer Hammann and his team of RV METEOR. Their great interest, intense support, and high expertise made this cruise (M110) a successful voyage. Two anonymous reviewers and the associate editor provided highly valuable comments for an improvement of the manuscript. The study is supported by the DFG Research Center/Excellence Cluster "The Ocean in the Earth System" (EXC309) at the University of Bremen and this article is a contribution to the MARUM-SD2 GALIOMAR project. All data derived from the cruise (M110) are summarized in the public-accessible cruise report through https://www.tib.eu/suchen/id/awi:doi:10.2312%252Fcr_m110/ and will be archived in PANGAEA (<https://doi.pangaea.de>) by September 2017. Before September 2017, the data are available from the authors upon request (wzhang@marum.de; thanebuth@marum.de).

References

- Allison, M. A., A. Sheremet, M. A. Goni, and G. W. Stone (2005), Storm layer deposition on the Mississippi-Atchafalaya subaqueous delta generated by Hurricane Lili in 2002, *Cont. Shelf Res.*, 25(18), 2213–2232.
- Baasch, B., H. Müller, F. K. J. Oberle, and T. von Dobeneck (2014), Inversion of marine multifrequency electromagnetic profiling data: A new approach to resolve surficial sediment stratification, *Geophys. J. Int.*, 200(1), 439–451.
- Bennett, S. J., J. S. Bridge, and J. L. Best (1998), Fluid and sediment dynamics of upper stage plane beds, *J. Geophys. Res.*, 103(C1), 1239–1274.
- Blumberg, A. F., and G. L. Mellor (1987), A description of a three-dimensional coastal ocean circulation model, in *Three-Dimensional Coastal Ocean Models*, vol. 4, pp. 1–16, edited by N. S. Heaps, AGU, Washington, D. C.
- Bursik, M. (1995), Theory of the sedimentation of suspended particles from fluvial plumes, *Sedimentology*, 42, 831–838.
- Cacchione, D. A., W. D. Grant, D. E. Drake, and S. Glenn (1987), Storm-dominated bottom boundary layer dynamics on the northern California continental shelf: Measurements and predictions, *J. Geophys. Res.*, 92(C2), 1817–182.
- Chen, H., X. Xie, W. Zhang, Y. Shu, D. Wang, T. Vandorpe, and D. Van Rooij (2016), Deep-water sedimentary systems and their relationship with bottom currents at the intersection of Xisha Trough and Northwest Sub-Basin, South China Sea, *Mar. Geol.*, 378, 101–113.
- Colby, B. R. (1956), Relationship of sediment discharge to stream-flow, *U.S. Geol. Surv. Open-File Rep.*, 56-27, 170 pp.
- Corbett, D. R., J. P. Walsh, C. K. Harris, A. S. Ogston, and A. R. Orpin (2014), Formation and preservation of sedimentary strata from coastal events: Insights from measurements and modelling, *Cont. Shelf Res.*, 86, 1–5.
- Csanady, G., and P. Shaw (1983), The insulating effect of a steep continental-slope, *J. Geophys. Res.*, 88(C12), 7519–7524.
- Dalrymple, R. W., and D. I. Cummings (2005), The offshore transport of mud: Why it doesn't happen and the stratigraphic implications [abs.], paper presented at Annual Conference, 20–22 Jun, Am. Assoc. of Pet. Geol./Soc. for Sediment. Geol. Calgary, Canada.
- Deng, J., W. Zhang, R. Schneider, J. Harff, J. Dudzinska-Nowak, P. Terfenko, A. Giza, and K. Furmanczyk (2014), A numerical approach for approximating the historical morphology of wave-dominated coasts: A case study of the Pomeranian Bight, southern Baltic Sea, *Geomorphology*, 204, 425–443.
- Dias, J. M. A., R. Gonzalez, C. Garcia, and V. Diaz-del-Rio (2002a), Sediment distribution patterns on the Galicia-Minho continental shelf, *Prog. Oceanogr.*, 52, 215–231.
- Dias, J. M. A., J. M. Jouanneau, R. Gonzalez, M. F. Araujo, T. Drago, C. Garcia, A. Oliveira, A. Rodrigues, J. Vitorino, and O. Weber (2002b), Present day sedimentary processes on the northern Iberian shelf, *Prog. Oceanogr.*, 52, 249–259.
- Egbert, G. D., and L. Erofeeva (2002), Efficient inverse modeling of barotropic ocean tides, *J. Atmos. Oceanic Technol.*, 19, 183–204.
- Fredsoe, J., and R. Deigaard (1992), *Mechanics of Coastal Sediment Transport: Advanced Series on Ocean Engineering*, World Sci., Singapore.
- Friedrichs, C. T., and L. D. Wright (2004), Gravity driven sediment transport on the continental shelf: Implications for equilibrium profiles near river mouths, *Coastal Eng.*, 51, 795–811.
- Gao, S., and M. B. Collins (2014), Holocene sedimentary systems on continental shelves, *Mar. Geol.*, 352, 268–294.
- Geyer, W. R., P. S. Hill, and G. C. Kineke (2004), The transport, transformation and dispersal of sediment by buoyant coastal flows, *Cont. Shelf Res.*, 24, 927–949.
- Grant, W. D., and O. S. Madsen (1979), Combined wave and current interaction with a rough bottom, *J. Geophys. Res.*, 84(C4), 1797–1808.
- Grant, W. D., and O. S. Madsen (1982), Movable bed roughness in unsteady oscillatory flow, *J. Geophys. Res.*, 87(C1), 469–481.
- Hale, R. P., and A. S. Ogston (2015), In situ observations of wave-supported fluid-mud generation and deposition on an active continental margin, *J. Geophys. Res. Earth Surf.*, 120, 2357–2373, doi:10.1002/2015JF003630.
- Hanebuth, T. J. J., and H. Lantzsich (2008), A Late Quaternary sedimentary shelf system under hyperarid conditions: Unravelling climatic, oceanographic and sea-level controls (Golfe d'Arguin, Mauritania, NW Africa), *Mar. Geol.*, 256(1–4), 77–89.
- Hanebuth, T. J. J., et al. (2007), Report and First Results of the POSEIDON Cruise 342 GALIOMAR – Galician Ocean Margin Expedition, Vigo (Spain) – Lisboa (Portugal), 19 Aug to 6 Sept 2006, *Ber. Fachbereich Geowissenschaften, Univ. Bremen*, 255, 203 pp.
- Hanebuth, T. J. J., et al. (2012), Cruise report and preliminary results RV METEOR Cruise M84/4 GALIOMAR III, Vigo – Vigo (Spain), 1–28 May 2011, *Ber. Fachbereich Geowissenschaften, Univ. Bremen*, 283, 139 pp.
- Hanebuth, T. J. J., et al. (2015a), GALIMOS: Monitoring the interaction between Oceanographic elements and Sedimentary seabed structures at the GALICIAN margin. RV METEOR cruise M110 GALIMOS, Sept. 15 – 30, 2014, Vigo (Spain) – Cádiz (Spain), *Meteor-Ber.*, M110, 69 pp, doi:10.2312/cr_m110.
- Hanebuth, T. J. J., W. Zhang, A. L. Hofmann, L. A. Löwemark, and T. Schwenk (2015b), Oceanic density fronts steering bottom-current induced sedimentation deduced from a 50-ka contourite drift record and numerical modelling (off NW Spain), *Quat. Sci. Rev.*, 112, 207–225.
- Hanebuth, T. J. J., H. Lantzsich, and J. Nizou (2015c), Mud depocenters on continental shelves – appearance, initiation times, and growth dynamics, *Geo-Mar. Lett.*, 35(6), 487–503.
- Harris, C. K., P. A. Traykovski, and R. W. Geyer (2005), Flood dispersal and deposition by near-bed gravitational flows and oceanographic transport: A numerical modeling study of the Eel River shelf, northern California, *J. Geophys. Res.*, 110, C09025, doi:10.1029/2004JC002727.
- Herrmann, M. J., and O. S. Madsen (2007), Effect of stratification due to suspended sand on velocity and concentration distribution in unidirectional flows, *J. Geophys. Res.*, 112, C02006, doi:10.1029/2006JC003569.
- Hill, P. S., and I. N. McCave (2001), Suspended particle transport in benthic boundary layers, in *The Benthic Boundary Layer: Transport Processes and Biogeochemistry*, edited by B. P. Boudreau and B. B. Jorgensen, pp. 78–103, Oxford Univ. Press, N. Y.
- Hooshmand, A., A. R. Horner-Devine, and M. P. Lamb (2015), Structure of turbulence and sediment stratification in wave-supported mud layers, *J. Geophys. Res. Oceans*, 120, 2430–2448, doi:10.1002/2014JC010231.
- Hsu, T. J., C. E. Ozdemir, and P. A. Traykovski (2009), High-resolution numerical modeling of wave-supported gravity-driven mudflows, *J. Geophys. Res.*, 114, C05014, doi:10.1029/2008JC005006.
- HydroQual, Inc. (2002), *A Primer for ECOMSED Version 1.3. (Computer Program Manual)*, Mahwah, N. J.
- Ichaso, A. A., and R. W. Dalrymple (2009), Tide and wave-generated fluid mud deposits in the Tilje Formation (Jurassic), offshore Norway, *Geology*, 37, 539–542.
- Kampf, J., and P. Myrow (2014), High-density mud suspensions and cross-shelf transport: On the mechanism of gelling ignition, *J. Sediment. Res.*, 84(3), 215–223.
- Kineke, G. C., R. W. Sternberg, J. H. Trowbridge and W. R. Geyer (1996), Fluid-mud processes on the Amazon continental shelf, *Cont. Shelf Res.*, 16, 667–696.
- Kineke, G. C., K. J. Woolfe, S. A. Kuehl, J. Milliman, T. M. Dellapenna, and R. G. Purdon (2000), Sediment export from the Sepik River, Papua New Guinea: Evidence for a divergent dispersal system, *Cont. Shelf Res.*, 20, 2239–2266.

- Lantzsch, H., T. J. J. Hanebuth, and V. B. Bender (2009), Holocene evolution of mud depocentres on a high-energy, low-accumulation shelf (NW Iberia), *Quat. Res.*, *72*(3), 325–336.
- Lantzsch, H., T. J. J. Hanebuth, and R. Henrich (2010), Sediment recycling and adjustment of deposition during deglacial drowning of a low-accumulation shelf (NW Iberia), *Cont. Shelf Res.*, *30*, 1665–1679.
- Macquaker, J. H. S., S. J. Bentley, and K. M. Bohacs (2010), Wave-enhanced sediment gravity flows and mud dispersal across continental shelves: Reappraising sediment transport processes operating in ancient mudstone successions, *Geology*, *38*, 947–950.
- McCalpin, J. (1994), A comparison of second-order and fourth-order pressure gradient algorithms in a s-coordinate ocean model. *Int. J. Numer. Meth. Fluids*, *18*, 361–383.
- McCave, I. N. (1973), Transport and escape of fine-grained sediment from shelf areas, in *Shelf Sediment Transport: Process and Pattern*, edited by D. J. P. Swift, D. B. Duane, and O. H. Pilkey, pp. 225–244, Dowden Hutchinson Ross, Stroudsburg, Pa.
- McKee, B. A., R. C. Aller, M. A. Allison, T. S. Bianchi and G. C. Kineke (2004), Transport and transformation of dissolved and particulate materials on continental margins influenced by major rivers: Benthic boundary layer and seabed processes, *Cont. Shelf Res.*, *24*(7–8), 899–926.
- Mellor, G. L., M. A. Donelan, and L. Y. Oey (2008), A surface wave model for coupling with numerical ocean circulation models, *J. Atmos. Oceanic Technol.*, *25*(10), 1785–1807.
- Moriarty, J. M., C. K. Harris, and M. G. Hadfield (2014), A hydrodynamic and sediment transport model for the Waipaoa shelf, New Zealand: Sensitivity of fluxes to spatially-varying erodibility and model nesting, *J. Mar. Sci. Eng.*, *2*(2), 339–369.
- Naughton, F., J. F. Bourillet, M. Fernanda, S. Goñi, J. L. Turon, and J. M. Jouanneau (2007), Long-term and millennial-scale climate variability in northwestern France during the last 8850 years, *Holocene*, *17*(7), 939–953.
- Nielsen, P. (1992), *Coastal Bottom Boundary Layers and Sediment Transport: Advanced Series on Ocean Engineering*, 4th ed., World Sci., Singapore.
- Nittrouer, C. A., and L. D. Wright (1994), Transport of particles across continental shelves, *Rev. Geophys.*, *32*(1), 85–113, doi:10.1029/93RG02603.
- Oberle, F. K. J., T. J. J. Hanebuth, B. Baasch, and T. Schwenk (2014), Volumetric budget calculation of sediment and carbon storage and export for a late Holocene mid-shelf mudbelt system (NW Iberia), *Cont. Shelf Res.*, *76*, 12–24.
- Ogston, A.S., D. A. Cacchione, R. W. Sternberg, and G. C. Kineke (2000), Observations of storm and river flood-driven sediment transport on the Northern California continental shelf. *Cont. Shelf Res.*, *20*, 2141–2162.
- Oliveira, A., J. Vitorino, A. Rodrigues, J. M. Jouanneau, J. A. Dias, and O. Weber (2002), Nepheloid layer dynamics in the northern Portuguese shelf, *Prog. Oceanogr.*, *52*, 195–213.
- Orpin, A. R. (2004), Holocene sediment deposition on the Poverty-slope margin by the muddy Waipaoa River, East Coast New Zealand, *Mar. Geol.*, *209*, 69–90.
- Otero, P., M. Ruiz-Villarreal, A. Peliz, and J. M. Cabanas (2010), Climatology and reconstruction of runoff time series in northwest Iberia: Influence in the shelf buoyancy budget off Ría de Vigo, *Sci. Mar.*, *74*(2), 1156–1180.
- Ozdemir, C. E., T. J. Hsu, and S. Balachandar (2010), A numerical investigation of fine particle laden flow in an oscillatory channel: The role of particle-induced density stratification, *J. Fluid Mech.*, *665*, 1–45.
- PO-WAVES Group (1994), Final report of sub-project A, Wind wave climatology of the Portuguese coast, *Rep. REL. FT. OM 5/94*, 106 pp., Inst. Hidrográfico, Lisbon.
- Quaresma, L. S., and A. Pichon (2013), Modelling the barotropic tide along the West-Iberian margin, *J. Mar. Syst.*, *109–110*, s3–s25.
- Relvas, P., E. D. Barton, J. Dubert, P. B. Oliveira, A. Peliz, J. C. B. da Silva, and A. M. P. Santos (2007), Physical oceanography of the western Iberia ecosystem: Latest views and challenges, *Prog. Oceanogr.*, *74*, 149–173.
- Richardson, J. F., and W. N. Zaki (1954), Sedimentation and fluidisation: Part 1, *Trans. Inst. Chem. Eng.*, *32*, 35–53.
- Rosenberg, R. (2001), Marine benthic faunal successional stages and related sedimentary activity, *Sci. Mar.*, *65*, 107–119.
- Schmidt, F., K. U. Hinrichs, and M. Elvert (2010), Sources, transport, and partitioning of organic matter at a highly dynamic continental margin, *Mar. Chem.*, *118*(1–2), 37–55.
- Scully, M. E., C. T. Friedrichs, and L. D. Wright (2003), Numerical modeling results of gravity-driven sediment transport and deposition on an energetic continental shelf: Eel River, Northern California, *J. Geophys. Res.*, *108*(C4), 3120, doi:10.1029/2002JC001467.
- Sommerfield, C. K., and R. A. Wheatcroft (2007), Late Holocene sediment accumulation on the northern California shelf: Oceanic, fluvial, and anthropogenic influences, *Geol. Soc. Am. Bull.*, *119*(9–10), 1120–1134.
- Sternberg, R. W., D. A. Cacchione, B. Paulso, G. C. Kineke, and D. E. Drake (1996), Observations of sediment transport on the Amazon sub-aqueous delta, *Cont. Shelf Res.*, *16*, 697–715.
- Sternberg, R. W., K. Aagaard, D. Cacchione, R. A. Wheatcroft, R. A. Beach, A. T. Roach, and M. A. H. Marsden (2001), Long-term near-bed observations of velocity and hydrographic properties in the northwest Barents Sea with implications for sediment transport, *Cont. Shelf Res.*, *21*, 509–529.
- Styles, R., and S. M. Glenn (2000), Modeling stratified wave and current bottom boundary layers on the continental shelf, *J. Geophys. Res.*, *105*(C10), 24,119–24,139.
- Syvitski, J. P., and M. D. Morehead (1999), Estimating river-sediment discharge to the ocean: Application to the Eel margin, northern California, *Mar. Geol.*, *154*, 13–28.
- Traykovski, P., W. R. Geyer, J. D. Irish, and J. F. Lynch (2000), The role of wave-induced density-driven fluid mud flows for cross-shelf transport on the Eel River continental shelf, *Cont. Shelf Res.*, *20*(16), 2113–2140.
- Traykovski, P., P. L. Wiberg, and W. R. Geyer (2007), Observations and modeling of wave-supported sediment gravity flows on the Po delta and comparison to prior observations from the Eel shelf, *Cont. Shelf Res.*, *27*, 375–399.
- Trowbridge, J. H. and G. C. Kineke (1994), Structure and dynamics of fluid muds on the Amazon continental shelf, *J. Geophys. Res.*, *99*(C1), 865–874.
- Walsh, J. P. and C. A. Nittrouer (2009), Understanding fine-grained river-sediment dispersal on continental margins, *Mar. Geol.*, *263*, 34–45.
- Warner, J. C., C. R. Sherwood, R. P. Signell, C.K. Harris, and H. G. Arango (2008), Development of a three-dimensional, regional, coupled wave, current, and sediment-transport model, *Comput. Geosci.*, *34*(10), 1284–1306.
- Wooster, W. S., A. Bakun, and D. R. McClain (1976), Seasonal upwelling cycle along eastern boundary of North-Atlantic, *J. Mar. Res.*, *34*(2), 131–141.
- Wright, L. D. (1977), Sediment transport and deposition at river mouths: A synthesis, *Geol. Soc. Am. Bull.*, *88*, 857–868.
- Wright, L. D., and C. T. Friedrichs (2006), Gravity-driven sediment transport on continental shelves: A status report, *Cont. Shelf Res.*, *2*, 2092–2107.
- Wright, L. D., C. T. Friedrichs, S. C. Kim, and M. E. Scully (2001), Effects of ambient currents and waves on gravity-driven sediment transport on continental shelves, *Mar. Geol.*, *175*(1–4), 25–45.

- van Rijn, L. C. (1993), *Principles of Sediment Transport in Rivers, Estuaries and Coastal Seas*, Aqua Publ., Amsterdam.
- Varban, B., and G. A. Plint (2008), Palaeoenvironments, palaeogeography, and physiography of a large, shallow, muddy ramp: Late Cenomanian–Turonian Kaskapau Formation, Western Canada foreland basin, *Sedimentology*, *55*, 201–233.
- Vitorino, J., A. Oliveira, J. M. Jouanneau, and T. Drago (2002a), Winter dynamics on the northern Portuguese shelf. Part 1: Physical processes, *Prog. Oceanogr.*, *52*(2), 129–153.
- Vitorino, J., A. Oliveira, J. M. Jouanneau, and T. Drago (2002b), Winter dynamics on the northern Portuguese shelf. Part 2: Bottom boundary layers and sediment dispersal, *Prog. Oceanogr.*, *52*(2), 155–170.
- Yalin, M. S. (1977), *Mechanics of Sediment Transport*, 298 pp., Pergamon, N. Y.
- Zhang, W., J. Harff, R. Schneider, and C. Y. Wu (2010), Development of a modeling methodology for simulation of long-term morphological evolution of the southern Baltic coast, *Ocean Dyn.*, *60*(5), 1085–1114.
- Zhang, W., R. Schneider, and J. Harff (2012), A multi-scale hybrid long-term morphodynamic model for wave-dominated coasts, *Geomorphology*, *149–150*, 49–61.
- Zhang, W., J. Deng, J. Harff, R. Schneider, and J. Dudzinska-nowak (2013), A coupled modeling scheme for longshore sediment transport of wave-dominated coasts: A case study from the southern Baltic Sea, *Coastal Eng.*, *72*, 39–55.
- Zhang, W., J. Harff, R. Schneider, M. Meyer, E. Zorita, and B. Hünicke (2014), Holocene morphogenesis at the southern Baltic Sea: Simulation of multiscale processes and their interactions for the Darss-Zingst peninsula, *J. Mar. Syst.*, *129*, 4–18.
- Zhang, W., R. Schneider, J. Kolb, T. Teichmann, J. Dudzinska-Nowak, J. Harff, and T. J. J. Hanebuth (2015), Land-sea interaction and morphogenesis of coastal foredunes: A modeling case study from the southern Baltic Sea coast, *Coastal Eng.*, *99*, 148–166.
- Zhang, W., T. J. J. Hanebuth, and U. Stöber (2016), Short-term sediment dynamics on a mesoscale contourite drift (off NW Iberia): Impacts of multi-scale oceanographic processes deduced from the analysis of mooring data and numerical modelling, *Mar. Geol.*, *378*, 81–100.